THESIS FOR THE DEGREE OF DOCTOR OF PHILOSOPHY

Understanding the interactions between vibrational modes and excited state relaxation in garnet structured phosphors

Yuan-Chih Lin

CHALMERS

Department of Chemistry and Chemical Engineering
CHALMERS UNIVERSITY OF TECHNOLOGY
Göteborg, Sweden 2018

Cover:
Close-up of the local coordination environment of the Ce^{3+} ion in an oxide garnet phosphor, illustrating the interactions between the excited state electron of Ce^{3+} and the vibrations of the surrounding O ligands.

Typeset in LaTeX. Figures created using IGOR Pro and Adobe Illustrator CC 2018.

Understanding the interactions between vibrational modes and excited state relaxation in garnet structured phosphors

Yuan-Chih Lin

Department of Chemistry and Chemical Engineering

Chalmers University of Technology

Abstract

This thesis concerns investigations of the local structural environments and vibrational dynamics of the three garnet type oxide phosphors Ce^{3+}-doped $Y_3Al_5O_{12}$ ($YAG:Ce^{3+}$), $Ca_3Sc_2Si_3O_{12}$ ($CSS:Ce^{3+}$), and $Sr_3Y_2Ge_3O_{12}$ ($SYG:Ce^{3+}$), which show promising optical properties as luminescent materials used in solid state white lighting technologies. The study focuses on a comprehensive analysis of the nature of the long-range vibrations (phonons) in terms of local atomic and molecular motions of the garnet structure, as well as their dependence on the nature of the garnet chemical composition, Ce^{3+} concentration and temperature. The aim is to understand how these materials properties affect key optical properties, such as the intensity and wavelength (color) of the emitted light. The investigations have been conducted by using a combination of Raman, infrared, luminescence, and neutron spectroscopies, together with mode-selective vibrational excitation experiments, and are further supported by theoretical and semi-empirical analyses and computer modeling based on density functional theory.

The results show that increasing the Ce^{3+} concentration and/or temperature cause(s) a red-shifting effect on the emission color due to an increased crystal field acting on the Ce^{3+} ions in $YAG:Ce^{3+}$. This is primarily attributed to the thermal excitation of certain high-frequency phonon modes that induce dynamical tetragonal distortions of the local CeO_8 moieties. A reversal (blue-)shift of the emission color observed at higher temperatures is, however, the result of counteracting thermal lattice expansion which turns the local coordination of CeO_8 into a more cubic symmetry. Specifically, it is found that the upward-shift of the frequencies of certain vibrational modes in $YAG:Ce^{3+}$ through decreasing the Ce^{3+} concentration or cosubstitution of smaller and/or lighter atoms on the Y sites increases the thermal stability of the emission intensity. This higher thermal stability of the emission intensity is attributed to a less activation of modes that give rise to nonradiative relaxation of electrons in the excited states *via* electron–phonon coupling and/or energy migration processes. For $SYG:Ce^{3+}$, the emission intensity is found to decrease strongly with increasing temperature, as a result of thermal ionization by promoting the electrons of Ce^{3+} ions into the conduction band of the host, followed by charge trapping at defects. $CSS:Ce^{3+}$ exhibits excellent thermal stability up to very high temperatures, 860 K.

Keywords: *phosphor, garnet, luminescence, vibrational spectroscopy, neutron scattering, free electron laser, light emitting diode, thermal quenching.*

List of publications

This thesis includes the following papers:

I **Inorganic Phosphor Materials for Lighting**
Yuan-Chih Lin, Maths Karlsson, and Marco Bettinelli
Topics in Current Chemistry, **374**, 1–47, (2016)
doi: 10.1007/s41061-016-0023-5

II **Understanding the Interactions between Vibrational Modes and Excited State Relaxation in $Y_{3-x}Ce_xAl_5O_{12}$: Design Principles for Phosphors Based on $5d$–$4f$ Transitions**
Yuan-Chih Lin, Paul Erhart, Marco Bettinelli, Nathan C. George, Stewart F. Parker, and Maths Karlsson
Chemistry of Materials **30**, 1865–1877, (2018)
doi: 10.1021/acs.chemmater.7b04348

III **Weak thermal quenching of the luminescence in the $Ca_3Sc_2Si_3O_{12}Ce^{3+}$ garnet phosphor**
Suchinder K. Sharma, Yuan-Chih Lin, Irene Carrasco, Tobias Tingberg, Marco Bettinelli, and Maths Karlsson
Journal of Materials Chemistry C **6**, 8923–8933, (2018)
doi: 10.1039/c8tc02907e

IV **Vibrational Tuning of Photoluminescence in Ce^{3+}-Doped Garnet Phosphors**
Yuan-Chih Lin, Paul Erhart, Marco Bettinelli, and Maths Karlsson
In manuscript

V **Thermal Quenching in the Yellow-Emitting Phosphor YAG:Ce^{3+}**
Yuan-Chih Lin, Marco Bettinelli, Suchinder K. Sharma, A. F. G. van der Meer, Britta Redlich, Adolfo Speghini, and Maths Karlsson
In manuscript

The author's contributions to the papers:

I The author prepared the first draft of the sections 1–4 of the paper and wrote the paper together with the other authors.

II The author performed all experimental and theoretical work excluding the DFT calculations. The author prepared the first draft of the paper and wrote the paper together with the other authors.

III The author performed all temperature dependent luminescence measurements and constructed the VRBE diagrams. The paper was written jointly with the other authors.

IV The author performed all experiments and theoretical analyses. The author prepared the first draft of the paper and wrote the paper together with the other authors.

V The author performed all experiments and the computational simulation. The author prepared the first draft of the paper and wrote the paper together with the other authors.

Other papers to which I have contributed to during my PhD studies, but that are not part of this thesis:

i **Structural and Vibrational Properties of Silyl (SiH_3^-) Anions in $KSiH_3$ and $RbSiH_3$: New Insight into Si–H Interactions**
Verina F. Kranak, Yuan-Chih Lin, Maths Karlsson, Janos Mink, Stefan T. Norberg, and Ulrich Häussermann
Inorganic Chemistry, **54**, 2300–2309, (2015)
doi: 10.1021/ic502931e

ii **Vibrational properties of β-$KSiH_3$ and β-$RbSiH_3$: a combined Raman and inelastic neutron scattering study**
Janos Mink, Yuan-Chih Lin, Maths Karlsson, Carin Österberg, Terrence J. Udovic, Henrik Fahlquist, and Ulrich Häussermann
Journal of Raman Spectroscopy, **48**, 284–291, (2017)
doi: 10.1002/jrs.5013

iii **Investigation of the Order–Disorder Rotator Phase Transition in $KSiH_3$ and $RbSiH_3$**
Reji Nedumkandathil, Aleksander Jaworski, Andreas Fischer, Carin Österberg, Yuan-Chih Lin, Maths Karlsson, Jekabs Grins, Andrew J. Pell, Mattias Edén, and Ulrich Häussermann
The Journal of Physical Chemistry C, **121**, 5241–5252, (2017)
doi: 10.1021/acs.jpcc.6b12902

Contents

Glossary

LED	Light emitting diode
RGB	Red, green, and blue
CCT	Correlated color temperature
CRI	Color rendering index
LER	Luminous efficacy of optical radiation
pc-WLED	Phosphor converted white light emitting diode
QE	Quantum efficiency
DFT	Density functional theory
EXAFS	Extended X-ray absorption fine structure
RT	Room temperature
DOS	Density of states
CB	Conduction band
VB	Valence band
VRBE	Vacuum referred binding energy
PDM	Phonon decomposition map
IR	Infrared
INS	Inelastic neutron scattering
EM	Electromagnetic
PL	Photoluminescence
TL	Thermoluminescence
FEL	Free electron laser
RF	Radio frequency
FTIR	Fourier transform infrared
CCD	Charge coupled device
CW	Continuous wave
FELIX	Free Electron Laser for Infrared eXperiments
Linac	Linear accelerator

Chapter 1

Introduction

Understanding the mechanistic aspects of the vibrational dynamics of atoms in materials has become an increasingly important field of research because it has shown to play a key role in determining several macroscopic (or functional) materials properties, such as ionic and electronic conductivity, hydrogen sorption, solar energy conversion, and luminescence, to name a few [1–7]. In crystalline materials, the vibrational dynamics is manifested as both localized dynamics of atoms and long-range collective motions of atoms in a specific manner based on the symmetry properties of the crystal structure, where a specific type of vibration is unique and characterized by its symmetry of motion, frequency and amplitude. These properties depend on the nature and local and long-range structural arrangement of the atomic species involved in the vibration. It follows that the study of vibrational dynamics can give important information about the structure of materials. In further detail, the excitation of specific vibrational modes induces structural dynamics which may affect the interaction between the material and particles such as impinging photons, electrons and protons, which often determines functional materials properties.

This thesis deals with the study of the interactions between vibrational dynamics and luminescence in inorganic phosphors, which are of relevance for the creation of environment friendly white lighting devices. These devices aim to replace the old and inefficient white lighting technologies that have been phased out (incandescent lamps) or are problematic from an environmental
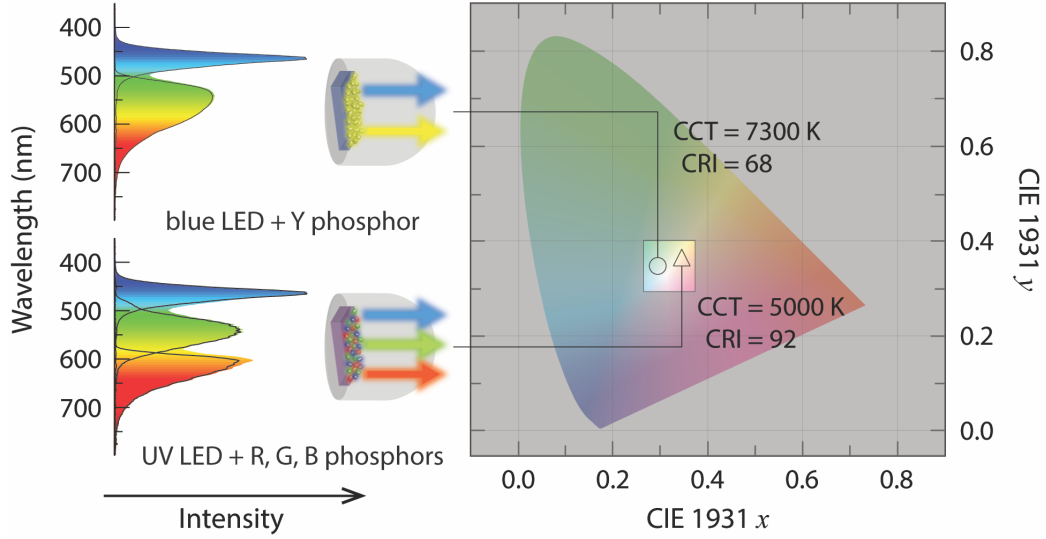
Figure 1.1: Schematic illustration of pc-WLED devices based on a blue LED chip coated with a Y phosphor, and an UV LED chip coated with R, G, and B phosphors, together with their emission spectra and color coordinates in a CIE 1931 diagram.

point of view (compact fluorescent lamps) [8,9]. Inorganic phosphors consist of a crystalline host lattice and a small concentration of activator ions (*e.g.* the lanthanides Ce^{3+}, Eu^{2+}, Pr^{3+}, and so forth), and when combined with a bright-blue LED (light emitting diode) [10,11], it may convert light from the LED into longer wavelengths. The admixture of different wavelengths results in white light emission. Most commonly, blue LEDs ($\approx$ 450–480 nm) can be used to excite either a yellow (Y) phosphor or a green (G) and a red (R) phosphor, whilst UV LEDs ($\approx$ 380–410 nm) are used to excite red (R), green (G) and blue (B) phosphors, to produce white light, see Figure 1.1.

The lighting characteristics are typically defined by the correlated color temperature (CCT), the color rendering index (CRI), and the luminous efficacy of optical radiation (LER). The CCT is a measure of the perceived color temperature of the emitted light compared to that of black-body radiation such as the radiation from the sun. The CRI is a parameter indicating the capability to reproduce colors of an object with respect to that as illuminated by a black-body radiation source. The LER is defined as the ratio of the total luminous flux (in lumens, lm) to radiant power (in watts, W),

where the luminous flux refers to the power of light perceived by the human eye. Therefore, the LER is a measure of the optical efficiency of the light emitted by a source, which can vary significantly in the range of 50–450 lm/W due to, *e.g.*, different operating currents and the package design of the device [12–15]. A low CCT (< 4000–5000 K) and a high CRI (close to 100) yield a warm, natural and comfortable white light emission spectrum (Figure 1.1), generally suited for, *e.g.*, indoor lighting.

Currently, one of the most widely used phosphor converted white LED (pc-WLED) technologies on the market is a blue LED coated with the yellow-emitting phosphor Ce^{3+}-doped yttrium aluminum garnet ($Y_{3-x}Ce_xAl_5O_{12}$, YAG:Ce^{3+}), which emits white light with a (relatively) high efficiency (up to 85 %) [16]. However, a major disadvantage of currently available devices is that the emitted white light comprises strong blue emission and hence is perceived as cold and unnatural. In comparison, pc-WLEDs based on an UV LED and a combination of R, G, and B phosphors produce a warmer white light, however these devices may suffer from technical complexity of mixing different phosphors onto LED chips, and low efficiency [17]. Furthermore, pc-WLEDs generally suffer greatly from thermal quenching, *i.e.* a pronounced reduction in emission intensity or internal and/or external quantum efficiency (QE)[1] of the phosphor(s), observed at elevated temperature, typically a few hundred degrees centigrade. To conclude, the trade-off between different measures, such as CCT, CRI, LER, QE, cost, fabrication and so forth, always presents and it is hardly satisfactory in all aspects [19, 20].

A promising means to tune the wavelength of the emitted light so that it is perceived as, *e.g.*, warmer and thus more suitable for indoor lighting, or so that the phosphor is more thermally stable, is to change the structural and dynamical properties at and around the luminescent ions [1, 21, 22]. However, the correlation between optical properties, local structure, and vibrational dynamics is, for virtually all known phosphors, far from fully understood. For this reason, this thesis aims to contribute with new understanding of the relation between local structure, vibrational dynamics, and luminescence performance of phosphors such as the color and intensity of the

---

[1]Internal QE = the number of emitted photons / the number of absorbed photons; External QE = the number of emitted photons / the number of incident photons. [18]

emitted light. The studies are focused both on the yellow-emitting phosphor YAG:Ce^{3+} and some other, green-emitting, Ce^{3+}-doped garnet phosphors, *i.e.* Ce^{3+}-doped $Ca_3Sc_2Si_3O_{12}$ and $Sr_3Y_2Ge_3O_{12}$ (CSS:Ce^{3+} and SYG:Ce^{3+}, respectively). The primary tools involve the use of infrared (IR), Raman, luminescence, and neutron spectroscopies together with computer modeling and also include the development of a new theoretical method to assign the local vibrations around the activator ions. Additionally, this thesis involves, for the first time, the use of monochromatic IR irradiation simultaneously with the electronic excitation of activator ions, for studying how certain vibrational modes couple to luminescence. The thesis provides unprecedented new insights into the relation between local structure and dynamics and macroscopic luminescence properties, such as the color and intensity of emitted light that are sensitive to local coordination environments.

Chapter 2

Inorganic phosphors

2.1 General aspects of luminescence

An inorganic phosphor consists of dilute activator ions and a host lattice that accommodates the activator ions. The activator ions absorb light of one wavelength (*e.g.* blue light, $\approx$ 450 nm). The absorbed energy is then turned into the emission of light of longer wavelength (*e.g.* yellow light, $\approx$ 550 nm) and into the excitation of vibrations of the host lattice which results in the heating of the material, see Figure 2.1(a). This process involves transitions between the electronic levels of the activator ions and between the vibrational states of the lattice, and may be described by a so called configurational coordinate diagram [Figure 2.1(b)]. The electronic transitions redistribute electrons between the ground- and excited-state configurations of the activator ions which correspond to the lower and upper parabolae in Figure 2.1(b). The electrons in the excited state configuration often relax to lower vibrational states before they radiatively return to the electronic ground state. This is manifested by the much shorter decay time of vibrational transitions (on the order of fs–ps) as compared to that of electronic transitions (on the order of ns) [23, 24]. This is in competition with the nonradiative process that occurs when excited-state electrons return to the electronic ground state through vibrational relaxation only. The electronic transitions are often characterized by the excitation (or absorption) and emission spectra whose shape and intensity are dictated by the probabil-
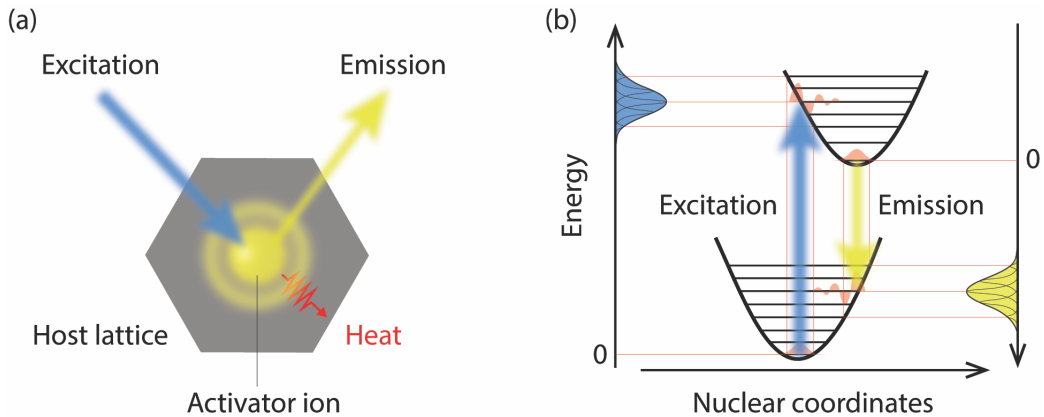
Figure 2.1: (a) A simple picture of a phosphor, which comprises one activator ion embedded in a host lattice. (b) Schematic principle of luminescence plotted in a configurational coordinate diagram in relation to excitation/absorption (blue) and emission (yellow) spectra. The parabolae represent the electronic state configurations while the horizontal lines refer to vibrational states in each electronic state.

ity of the optical transitions between the initial and final states based on the FranckCondon principle [23,24]. This principle establishes that an electronic transition occurs almost instantaneously without changing the positions of the nuclei of the molecular (vibrational) units involving the activator ions and their surroundings. This results in a vertical transition, which is also called a vibronic transition since it involves the instantaneous changes in both electronic and vibrational energy levels of the molecules. The shape of the spectrum arising from vibronic transitions is determined by the square of the overlap integral of the vibrational wave functions in the two electronic states, *cf.* red areas in Figure 2.1(b), whereas the intensity of the spectral bands is governed by the parity and spin selection rules for the transition between the electronic states, which is forbidden when the initial and final electronic states of the transition have the same parity and/or different spin states, and *vice versa* [23–25]. The degree of overlap between the wave functions in the electronic ground- and excited-state configurations depends on the difference in the bond length and strength of the activator ion and ligand pairs between the two electronic configurations. The bond length and strength determine the equilibrium positions and curvature of the respective parabolae, as shown

in Figure 2.1(b). For instance, an increased difference in the bond length between the ground- and excited-state configurations increases the complexity of vibronic transitions (*i.e.* enhanced coupling between the electronic and vibrational states), which gives rise to spectral broadening.

Strategies to tune the luminescence properties of inorganic phosphors involve the careful choice of activator ions and host material [21, 22, 26]. Examples of host materials for absorbing blue light and emitting green-yellow light are oxide aluminates (*e.g.* $Y_3Al_5O_{12}$ [27] and $LaSr_2AlO_5$ [28]), silicates (*e.g.* $Ca_3Sc_2Si_3O_{12}$ [29] and Sr_3SiO_5 [30,31]), germanates (*e.g.* $Sr_3Y_2Ge_3O_{12}$ [32]), oxynitrides (*e.g.* $Y_3Al_{5-x}Si_xO_{12-x}N_x$ [33, 34] and $Ca_3Sc_2Si_3O_{12-6x}N_{4x}$ [35]), nitrides (*e.g.* $CaAlSiN_3$ [36] and $SrAlSi_4N_7$ [37]), and oxyfluorides (*e.g.* $Sr_3Al_{1-x}Si_xO_{4+x}F_{1-x}$ [38]), doped with Ce^{3+} ions. The currently most important class of hosts of technological importance is the oxide garnets, which in general show high chemical, photochemical, and structural stability [22].

2.2 Oxide garnet phosphors

2.2.1 Garnet crystal structure

The general formula of garnet structured crystals may be expressed as $A_3B_2C_3O_{12}$, where A, B and C are cations at different sites, and O is oxygen. The garnet structure is classified into the space group of $Ia\bar{3}d$ (O_h^{10}), which is a 160-atom body-centered cubic unit cell [Figure 2.2(a)] [39]. The A, B, C, and O atoms occupy Wyckoff positions $12c$, $8a$, $12d$, and $48h$, respectively, which are assigned to D_2, S_6, S_4, and C_1 site symmetries, respectively [40]. The three different sites at which the A, B, and C cations occupy are 8-fold, 6-fold, and 4-fold coordinated to the neighboring O atoms, respectively. Thus, the garnet structure is built up of AO_8 dodecahedra, BO_6 octahedra, and CO_4 tetrahedra [Figure 2.2(a)]. The AO_8 dodecahedra may be viewed as distorted cubes, *i.e.* the symmetry of the AO_8 dodecahedra is distorted from the cubic point group symmetry O_h, see Figure 2.2(b). The BO_6 octahedra and CO_4 tetrahedra have slightly lowered symmetries with respect to regular octahedra and tetrahedra which are assigned to the point group symmetry
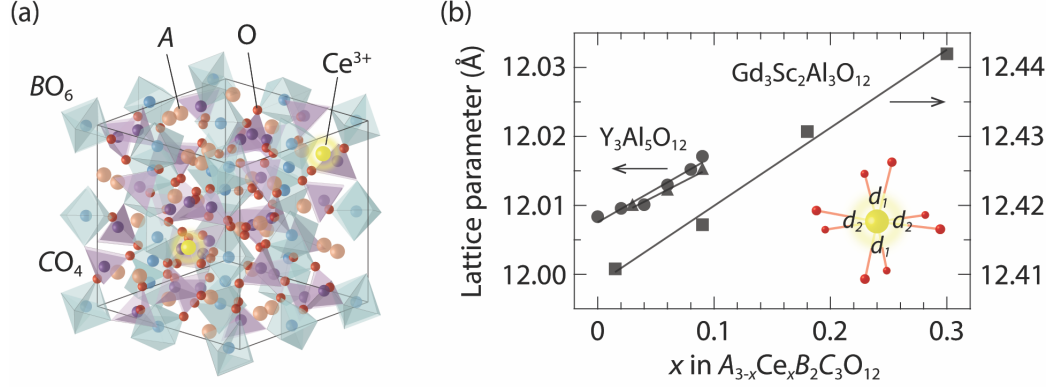
Figure 2.2: (a) Illustration of an unit cell of a $A_3B_2C_3O_{12}$ garnet crystal, as doped with Ce^{3+} ions at the A sites. (b) Lattice expansion of the Ce^{3+}-doped $Y_3Al_5O_{12}$ (filled circle and triangle) and $Gd_3Sc_2Al_3O_{12}$ (filled square) garnet phosphors upon increasing Ce^{3+} concentration, reproduced from [42–44]. Inset: a close-up of the local coordination of the Ce^{3+} ion in the garnet structure. The atomic distances of the first shell (Ce–O) and the second shell (Ce–O) are labelled by d_1 and d_2, respectively.

O_h and T_d, respectively. The degree of distortions of these polyhedra varies from one garnet to another one [32, 41].

Regarding the rare-earth or lanthanide doped forms of the garnets, the site occupation of the dopants may, *a priori*, be judged by comparing the ionic radii and charge states between Ce^{3+} and the cations they replace. For example, for YAG:Ce^{3+}, the Ce^{3+} ions substitute for Y^{3+} ions since their similar ionic radii in 8-fold coordination are very similar (Ce^{3+}: 1.143 Å, and Y^{3+}: 1.019 Å) and their charge states are identical [14, 45]. Similarly, for CSS:Ce^{3+}, the Ce^{3+} ions tend to substitute for Ca^{2+} ions due to comparable ionic radii (Ce^{3+}: 1.143 Å, and Ca^{2+}: 1.12 Å), however, two Ce^{3+} ions are expected to substitute for three Ca^{2+} ions to maintain charge neutrality, thus creating cation vacancies as "charge compensators". Other ions may be simultaneously added to increase the site occupation of the dopants. For instance, the amount of the Ce^{3+} ions on the Ca^{2+} site in the $Ca_3Sc_2Si_3O_{12}$ host is increased by replacing Sc^{3+} and Ca^{2+} ions with Mg^{2+} and Na^+/Li^+ ions, respectively [46].

Results obtained from extended X-ray absorption fine structure (EXAFS) experiments have shown that the lattice environment around Ce^{3+} is ex-

panded upon increasing Ce^{3+} concentration in YAG:Ce^{3+} [42, 47]. The expansion is found to be smaller at outer shells (1st O shell: 3.9 %, 2nd O shell: 2.5 %, 3rd Al shell: 1.6 %, and so forth [42]), implying that the distortions due to the mismatch of the ionic radii of Ce^{3+} and Y^{3+} ions are rather localized around Ce^{3+}. However, the expansion of the Ce–O bonds in the first shell is still smaller than expected based on the fact that Ce^{3+} is about 12% larger than Y^{3+} in 8-fold coordination, which suggests that the YAG lattice is a rigid structure against Ce^{3+} substitution and the local structure around the Ce^{3+} ions in YAG:Ce^{3+} is tightly compressed [42]. The effect of the local lattice expansion is, however, spread out through the whole unit cell (*i.e.* the averaged structure), as reflected by the increase of the lattice parameter upon increasing Ce^{3+} concentration in Ce^{3+}-doped YAG and $Gd_3Sc_2Al_3O_{12}$ [42–44], see Figure 2.2(b). The linear increase of the lattice size follows the Vegard law [48].

Various combinations of different atoms at the three cation sites (A, B, and C) in the solid solution of oxide garnet phosphor provides a remarkable flexibility of tuning the luminescence properties. A systematic method for cation substitution may be divided into three routes [22]: **i)** to substitute A atoms, *e.g.* (Y, Tb, Gd, Lu)$_3$Al$_5$O$_{12}$ [16, 49–51], **ii)** to substitute B and C atoms, *e.g.* (Y, Gd)$_3$Al$_{5-x}$Ga$_x$O$_{12}$ [41, 52], Y$_3$Sc$_2$Al$_{3-x}$Ga$_x$O$_{12}$ [53, 54], and (Y, Lu)$_3$Al$_{5-2x}$Mg$_x$Si$_x$O$_{12}$ [55–57], and **iii)** to substitute A (involving trivalent and/or divalent states), B and C atoms,*e.g.* silicates Ca$_3$Sc$_2$Si$_3$O$_{12}$ [14,29], Sr$_3$Y$_2$Ge$_3$O$_{12}$ [14], Ca$_2$GdZr$_2$Al$_3$O$_{12}$ [58], (Ca$_{1-x}$Sr$_x$)$_3$(Y, Lu)$_2$Ge$_3$O$_{12}$ [32], and Ca$_x$(Y, Lu)$_{3-x}$Al$_{5-x}$Si$_x$O$_{12}$ [59,60].

2.2.2   Energetics of the activator ion

The Ce ions often have the oxidation state +3 with the ground-state electronic configuration [Xe]$4f^1 5d^0$. The electron at the $4f$ ground state configuration can be promoted to the $5d$ excited state configuration upon the irradiation with light, which may be followed by a relaxation to the $4f$ configuration and the concomitant emission of light of longer wavelength. This is known as inter-configurational $4f$–$5d$ optical transitions, which give rise to intense and fast photoluminescence since they are parity and spin al-

Figure 2.3: The $4f$ and $5d$ electronic state configurations of a free Ce^{3+} ion, as well as when embedded in an oxide garnet host (*left*), in relation to the photoluminescence spectra of YAG:Ce^{3+} (*right*) as an example.

lowed [61, 62]. The $5d \rightarrow 4f$ emission of Ce^{3+} generally has a decay time of the order <100 ns [16]. The $4f$–$5d$ transitions lead to broadband photoluminescence excitation and emission spectra due to a wide range of vibronic transition energies, *i.e.* strong electron–phonon coupling. The electron–phonon coupling originates from the large change of the Ce–O distances and bond strength between the $4f$ and $5d$ states, as shown in the configurational coordinate diagram in Figure 2.1(b) [23, 63].

The transition energy between the $4f$ ground level and the lowest $5d$ level of a free gaseous Ce^{3+} ion is ∼6.12 eV, which is in the UV region, whereas it is mostly located in the blue-to-yellow region when the Ce^{3+} ion is incorporated into a garnet structured crystal [64]. The shifting from the UV to visible regions originates from the interaction of Ce^{3+} with its local coordination environment, which results in the so called centroid shift and crystal field splitting [27, 64]. These two effects are found to influence critically the $5d$ configuration energy of Ce^{3+}, since the outer $5d$ orbitals strongly interact with the local surroundings. Their magnitude is usually quantified by the decreasing energy (red-shift) of the lowest $5d$ level compared to the free Ce^{3+} ion state, $D(A)$ where A refers to a specific host (Figure 2.3) [24, 64].

The centroid shift ε_c refers to a lowering of the average energy of the

$5d$ levels as a result of the reduction of the Coulomb repulsion between the electrons of the Ce^{3+} ion [Figure 2.3]. The magnitude of ε_c is primarily determined by the covalency of the crystal (generally known as the nephelauxetic effect) and the polarizability of the anion ligands (*i.e.* of the oxygen atoms in the case of oxide phosphors) [27,64–66]. A high degree of covalency of the Ce–O bonds and strong anion polarizability tend to stabilize the $5d$ orbitals and hence increase ε_c.

The crystal field splitting refers to the energy separation between the highest and lowest $5d$ levels. The energy separation stems from the electrostatic field generated by the surrounding anion ligands and the interactions between the bonding orbitals [67,68]. Crucially, the magnitude of the crystal field splitting is related to the orbital overlap of the O anions with Ce^{3+}, the Ce–O bond lengths, and the symmetry of the CeO_8 moieties in the crystal. For the 8-fold cubic (cubal) coordination, the $5d$ levels of Ce^{3+} are split into a higher energy triplet level $^2T_{2g}$ and a lower energy doublet level ^2E_g. The $^2T_{2g}$ and ^2E_g levels are separated by an energy of $\Delta = (8/9)\cdot10Dq$ [Figure 2.3], where the coefficient $(8/9)$ is a conversion ratio of the cubal and octahedral coordinations ($\Delta \equiv 10Dq$ for the octahedral coordination), and Dq is a measure of the energy separation for the $5d$ orbitals which may be derived from the following relationship:

$$Dq = \frac{Ze^2r^4}{6R^5}. \qquad (2.1)$$

Here Dq is a product of the parameters D ($\propto Ze^2/R^5$) and q ($\propto r^4$), Z is the valence of the anion, e is the electric charge of an electron, r is the radius of the d-orbital wavefunction, and R is the bond length between Ce^{3+} and the coordinating O anions (ligands) [63,69,70]. In oxide garnets, Ce^{3+} substitutes for the atoms occupying at the sites with D_2 8-fold oxygen coordination (or dodecahedral coordination) which can be viewed as a tetragonally distorted cube. This type of lattice distortion lowers the symmetry of CeO_8 and gives rise to a tetragonal crystal field, which further splits the $^2T_{2g}$ and ^2E_g levels of Ce^{3+} into five non-degenerate levels. The magnitude of the tetragonal crystal field splitting can be estimated by the energy separation of the two lowest $5d$ levels ($5d_1$ and $5d_2$), Δ_{12} [Figure 2.3] [64].

Due to the unusually large crystal field splitting for most Ce^{3+}-doped garnet phosphors, the transition from the $4f$ level to the lowest $5d$ level ($5d_1$) of Ce^{3+} can be often driven by the irradiation of light in the blue region of the visible spectrum. The excited electron then energetically relaxes to the lower $5d_1$ level through electron–phonon coupling and the lattice vibrations surrounding Ce^{3+} ions reach a new equilibrium position, see Figure 2.1(b). This is followed by $5d_1 \rightarrow 4f$ transitions, which may result in green-yellow emission. The difference between the excitation and emission energies is known as the Stokes shift, ΔS. The magnitude of ΔS can be estimated by the energy difference between the maxima of the excitation and emission spectral bands (Figure 2.3), which usually falls in the range of 2000–4000 cm^{-1} [71, 72].

In contrast to the $5d$ electronic configuration, the $4f$ electronic configuration of Ce^{3+} is almost unaffected by the surrounding oxygen ligands since the $4f$ electrons are well shielded by the outer filled $5s$ and $5p$ shells of electrons. Instead, they are influenced by spin-orbit coupling (*i.e.* the interaction between the magnetic dipole of the spinning electron and the magnetic field due to the relative orbtial motion of the nucleus and electron) [63], which splits the $4f$ configuration into the lower energy $^2F_{5/2}$ level and higher energy $^2F_{7/2}$ level [Figure 2.3]. In accordance with the Dieke diagram [24, 63], the energy separation between the $^2F_{5/2}$ and $^2F_{7/2}$ levels of Ce^{3+} in garnets is found to take on a value of around 2000 cm^{-1} [14, 68, 73]. Since the separation of the two ^2F levels is relatively small, the two emission bands corresponding to the transitions from the $5d_1$ level to the $^2F_{5/2}$ level and to the $^2F_{7/2}$ level are generally manifested as a doublet band at low temperatures [74]. Further details about the centroid shift and tetragonal crystal field splitting that determine the luminescence characteristics of phosphors are given below.

2.2.3 Centroid shift

The centroid shift ε_c can be determined both experimentally and theoretically. Experimentally, ε_c is obtained from the difference between the average energies of all $5d$ levels in the free ion state and in the non-degenerate state (Figure 2.3), which are measured by excitation/absorption spectroscopy

[22, 65]. Theoretically, two different models are often used to estimate the magnitude of ε_c; these are the so called covalency model and ligand polarization model, which are described in the following.

The covalency model. The magnitude of ε_c has been shown to generally follow the order of $F^- < O^{2-}$ (sulfates < carbonates < phosphates < hydrated compounds < borates < silicates < aluminates) $< N^{3-}$ due to the nephelauxetic effect, which originates from an expansion of the electron cloud and thus an increased degree of donating electrons toward Ce^{3+} [22,65,66,75]. As a result, the Coulomb repulsion between the electrons of Ce^{3+} is reduced. This reduction may be explained using the covalency model, which correlates ε_c with the overlapping integral between the $5d$ orbital of Ce^{3+} and the ligands, as follows [61, 66]:

$$\epsilon_c = \beta \sum_{i=1}^{N} \exp\{-[R_i - (1/2)\Delta R]/b\}. \tag{2.2}$$

Here β is regarded as a measure of the covalency of the Ce–ligand bonds, N is the coordination number (*i.e.* 8 for Ce^{3+} on the A sites), R_i is the distance between Ce^{3+} and the ith ligand, ΔR refers to the lattice relaxation around Ce^{3+}, and b is a fitting parameter. The model reveals that higher covalency (the sharing of electrons) and shorter distances between Ce^{3+} and its ligands lead to a larger ε_c. The covalency tends to be lowered when the electron cloud of the ligands is strongly attracted by other cations than Ce^{3+} in the host, which generates a more ionic surrounding for Ce^{3+} [66].

Examples of using the covalency model are given as follows. In the aluminate garnet phosphors Ce^{3+}-doped $(Y, Lu, Gd)_3Al_5O_{12}$, the N^{3-} substitution for O^{2-}, which is usually accompanied with Si^{4+} (acting as a charge compensator to maintain charge neutrality) substitution for Al^{3+}, has shown a significant red-shifting effect on the photoluminescence of the $4f$–$5d_1$ transitions of Ce^{3+} ions. The red-shift is evident from the enhancement of the lower energy excitation/absorption and emission bands [33, 34, 76], which have been associated with the Ce^{3+} sites coordinating to N^{3-}, see Figure 2.4. This selective coordination may be attributed to the size-mismatch between the Al^{3+}–O^{2-} and smaller Si^{4+}–N^{3-} pairs since the larger Ce^{3+} ion prefers to
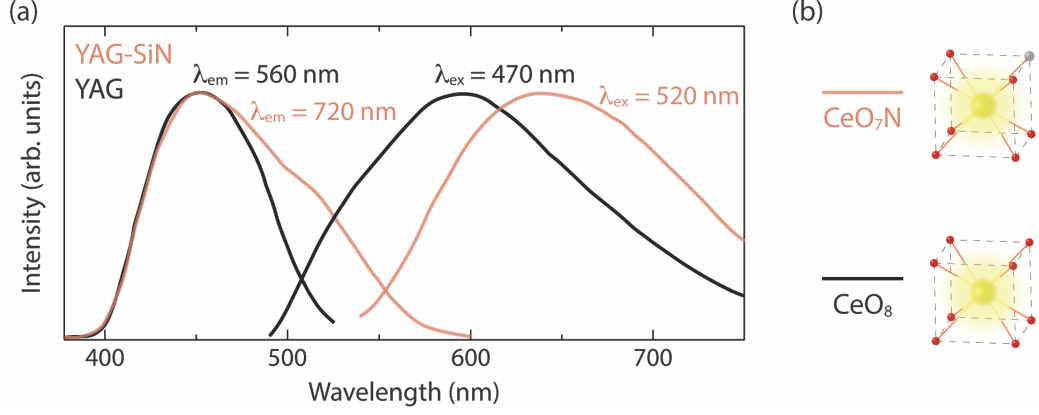
Figure 2.4: (a) Room temperature (RT) excitation and emission spectra of $Y_{2.91}Ce_{0.09}Al_{4.9}Si_{0.1}O_{11.9}N_{0.1}$ (YAG-SiN:3%Ce^{3+}), *i.e.* when N^{3-} coordinates to the Ce^{3+} ions, and $Y_{2.91}Ce_{0.09}Al_5O_{12}$ (YAG:3%Ce^{3+}), adapted from [33]. (b) Illustration of the local coordination around Ce^{3+} in YAG with and without N^{3-} in its coordination.

coordinate to N^{3-} in order to release the lattice stress created by the Ce^{3+} doping [77]. The $5d_1$ level of Ce^{3+} on these sites is distinguished from those with only O^{2-} in its nearest coordination shells and tends to be lower since ε_c turns to be larger when O^{2-} is replaced by N^{3-}. This is mainly the result of an increase of the covalency and anion polarizability. The similar red-shift is also observed for the N^{3-} substitution in the silicate garnet phosphor Ce^{3+} doped $Ca_3Sc_2Si_3O_{12}$ while O vacancy and Si^{4+} substitution for Sc^{3+} act as charge compensators [35]. In other oxynitride phosphors such as $M_{1.95}$ $Eu_{0.05}Si_{5-x}Al_xN_{8-x}O_x$ (M = Ca, Sr, and Ba), the size mismatch between the host cation M^{2+} and activator ion Eu^{2+} has also shown an effect of tuning the local chemical environments [78]. The AlO^+ substitution for SiN^+ leads to local clustering of N^{3-} around Eu^{2+} when M^{2+} is larger than Eu^{2+}, *i.e.* M = Ba or Sr. Such N^{3-} rich coordination accounts for the red-shift of the photoluminescence of the Eu^{2+} dopant.

The ligand polarization model. ε_c may be also contributed from the effect of ligand polarization. This results from a physical process that the $5d$ electrons of Ce^{3+} polarizes the electrons of the ligands, which gives rise to a reversed interaction with Ce^{3+}. This induces a potential to decrease the interelectron Coulomb repulsion [65, 66]. An analytical approximation

for the ligand polarization model may be expressed as

$$\varepsilon_c = \frac{e^2}{4\pi\epsilon_0}(\langle r^2 \rangle_{5d} - \langle r^2 \rangle_{4f}) \sum_{i=1}^{N} \frac{\alpha_i}{[R_i - (1/2)\Delta R]^6}. \qquad (2.3)$$

Here e is the charge of an electron, ϵ_0 is the permittivity of vacuum, r is the position of the electron, $\langle r^2 \rangle_{5d}$ and $\langle r^2 \rangle_{4f}$ are the expectation values of r^2 for the $5d$ and $4f$ orbitals, respectively, α_i is the polarizability of the ith ligand in the unrelaxed lattice, while the other variables (N, R_i, and ΔR) refer to the same quantities as in Equation 2.2. By assuming that the contribution from the covalency effects to ε_c is negligible, α_i can be replaced by the spectroscopic polarizability α_{sp} for all ligands, which can be derived from spectroscopic data [66]. For oxides, α_{sp} goes as χ_{av}^{-2}, where χ_{av} (the so called average cation electronegativity) is defined as follows [65]:

$$\chi_{av} = \frac{\sum_{i=1}^{N_c} z_{ci}\chi_{ci}}{\sum_{i=1}^{N_a} z_{ai}}. \qquad (2.4)$$

Here N_c and N_a are the numbers of cations and anions, respectively, while z_{ci} and z_{ai} are their respective valence charges and χ_{ci} is the corresponding cation electronegativity [79]. The relation between α_{sp} and χ_{av} physically implies that if the cation electronegativity is small the attraction of the anion electron cloud by other cations than Ce^{3+} is weak, which leads to small binding force constants of the electrons and thereby large anion polarizability. Therefore, it may be concluded from Equation 2.3 and 2.4 that smaller χ_{av} and shorter R_i results in larger ε_c.

Examples of using the ligand polarization model are given as follows. The Ce^{3+} doped silicate and germanate garnet phosphors have been generally suggested to exhibit a smaller centroid shift of the $5d$ levels than the aluminate based ones [80, 81]. This may be attributed to the larger electronegativity for Si^{4+} ($\chi_{Si} = 1.90$) and Ge^{4+} ($\chi_{Ge} = 2.01$) in comparison with Al^{3+} ($\chi_{Al} = 1.61$), which reduces the covalent character of the host material and the polarizability of the O anions coordinating to Ce^{3+}. How-

ever, the charge imbalance resulting from the Si^{4+}/Ge^{4+} substitution for Al^{3+} is usually compensated by the cosubstitution of Mg^{2+} ($\chi_{Mg} = 1.31$) for Al^{3+}, which contributes an increases of the covalency instead, for example, in $Y_3Al_{5-2y}(Mg, Si)_yO_{12}:Ce^{3+}$ [56]. The similar effect on the covalency is also observed for the Mg^{2+} substitution for Sc^{3+} ($\chi_{Sc} = 1.36$) in $(Ca, Lu)_3Sc_{2-y}Mg_ySi_3O_{12}:Ce^{3+}$ [82]. In the same material, Ca^{2+} ($\chi_{Ca} = 1.00$) is suggested to contribute more covalent character than Lu^{3+} ($\chi_{Lu} = 1.27$) [82]. The overall effect of the double cosubstitution of Mg^{2+}–Si^{4+} and Ca^{2+}–Si^{4+} pairs for Al^{3+}–Al^{3+} and Lu^{3+}–Al^{3+} pairs, respectively, in the host $Lu_3Al_5O_{12}$ appears to lower the covalency and reduce ε_c of Ce^{3+}, see the example of the Ce^{3+} doped $Lu_2CaMg_2Si_3O_{12}$ ($\varepsilon_c = 13300$ cm^{-1}) and $Lu_3Al_5O_{12}$ ($\varepsilon_c = 14300$ cm^{-1}) [80]. This may be attributed to the higher valence charge of Si^{4+} as compared to that of Mg^{2+} and Ca^{2+}, together with the fact that the electronegativity increment ($\chi_{Si} - \chi_{Al}$) and decrement ($\chi_{Mg} - \chi_{Al}$ and $\chi_{Ca} - \chi_{Lu}$) due to the double cosubstitution are comparable. As a result, χ_{av} is increased, which lowers the anion polarizability and hence leads to smaller ε_c (Equation 2.3 and 2.4).

To conclude, the centroid shift plays an important role in determining the photoluminescence excitation and emission wavelengths (colors), which depends on not only the activator ion itself but also on the surrounding anions and cations, *i.e.* on the host material. Both models mentioned above are very useful tools for the future design of new compounds when it comes to color tuning of photoluminescence.

2.2.4 Tetragonal crystal field

The tetragonal crystal field Δ_{12} (Figure 2.3) is predominantly affected by the local structural distortion of the CeO_8 moieties away from perfect cubic symmetry. It is sensitive to structural changes at the A, B, and C sites of the $A_3B_2C_3O_{12}$ garnet structure.

Substitution on the A sites. The replacement of the A cations with larger cations generally results in an increase of the tetragonal crystal field splitting. Thus, the luminescence of the Ce^{3+} $4f$–$5d_1$ transitions exhibits a red-shifting effect, as observed, *e.g.*, in the series of the hosts (Y, Gd,

Tb, $Lu)_3Al_5O_{12}$, whose local bond lengths in 8-fold coordination show a relation of Gd–O > Tb–O > Y–O > Lu–O [43, 49–51, 74, 83–86]. The substitution of larger cations is thought to enhance tetragonal distortions of the CeO_8 moieties, which leads to an increase of Δ_{12}, $i.e.$ to a lowering of the $5d_1$ level. Similarly, the replacement of Ca^{2+} (1.12 Å) with larger Sr^{2+} (1.26 Å) in 8-fold coordination [45] in the Ce^{3+} and Li^+ co-doped (Ca, $Sr)_3(Y, Lu)_2Ge_3O_{12}$ garnet phosphors may account for an observed red-shift of the emission [32]. Interestingly, an increase of the Ce concentration x in (Y, Gd, Tb, $Lu)_{3-x}Ce_xAl_5O_{12}$ garnet phosphors, where the Ce^{3+} ion is the largest compared to the other cations on the A sites, also exhibits a red-shift [49, 87]. This has been attributed to energy transfer among Ce^{3+} ions from higher to lower energy sites, which is a common feature of highly doped phosphors [36, 87, 88]. The lower energy sites may be related to the relatively compressed local environments around Ce^{3+}, which are expected to increase the crystal field splitting, Δ and/or Δ_{12} [1, 42].

Substitution on the B and/or C sites. The replacement of the B and/or C cations with larger cations, $e.g.$ Ga substitution for Al in the hosts (Y, $Gd)_3(Al, Ga)_5O_{12}$ [41, 52, 89], and $Y_3Sc_2(Al, Ga)_3O_{12}$ [53, 54], however, exhibits a blue-shift due to a decrease of Δ_{12} that often refers to the energy difference between the maxima of the $4f \rightarrow 5d_1$ and $4f \rightarrow 5d_2$ excitation bands. This has been explained by the fact that the tetragonally distorted coordination of the CeO_8 moiety shifts towards more cubic symmetry as the local lattice expands with increasing the Ga substitution. To measure the degree of tetragonal distortions, a distortion parameter is used, which is defined as the ratio of the two O–O edges of the dodecahedral moiety, d_{88}/d_{81} [Figure 2.5(a)]. In the Ce^{3+} doped $Y_3(Al, Ga)_5O_{12}$ garnet phosphors, the decrease of d_{88}/d_{81} ($i.e.$ less tetragonal distortions) due to the Ga substitution has been correlated with a simultaneous blue-shift of the emitted light [41].

Theoretical interpretation supported by experimental cases. To correlate the local structural distortions of the CeO_8 moieties to the tetragonal crystal field splitting, the distortions of a single, isolated, CeO_8 moiety may be theoretically treated and interpreted as different types of deformations with specific symmetries. Ab $initio$ calculations have indicated that there are two types of local lattice deformations of a CeO_8 cluster embedded
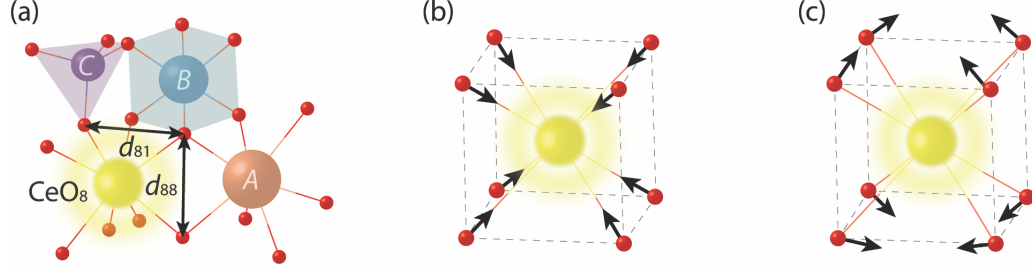
Figure 2.5: (a) Schematic illustration of the O–O edges d_{88} and d_{81} of the dodecahedral moiety in a garnet structure. d_{88} is the edge shared between two neighboring CeO_8/AO_8 dodecahedra, and d_{81} is the shortest unshared edge [90]. (b–c) Schematic illustration of tetragonal distortions of a cubic AO_8, assigned to (b) symmetric compression (A_{1g} symmetry) and (c) symmetric bending (E_g symmetry), respectively.

in a garnet host are associated with the enhancement of tetragonal distortions and hence these lead to a red-shift of the $5d_1 \rightarrow 4f$ emission of the Ce^{3+} ion [91, 92]. Specifically, these are the symmetric A_{1g} compression and symmetric E_g bending of the Ce–O bonds, see Figure 2.5(b) and (c), respectively. This theoretical result is in line with the experimental argument in regard to Ga substitution in the aluminate garnets, see above. Moreover, some studies have attributed a lowering of the Ce^{3+} $5d_1$ level to an enhanced compression of the local coordination around Ce^{3+} (as inferred from the shrinkage of the lattice), which results from cation substitutions, $e.g.$ the substitution of Al^{3+} for Sc^{3+} in $Ca_3(Sc, Al)_2Si_3O_{12}:Ce^{3+}$ [93] and the double substitution of Lu^{3+} and Mg^{2+} for Ca^{2+} and Sc^{3+}, respectively, in $(Ca, Lu)_3(Sc, Mg)_2Si_3O_{12}:Ce^{3+}$ [82]. An increase of Δ_{12} was also observed with increasing hydrostatic pressure in $Gd_3Ga_5O_{12}:Ce^{3+}$, which shortens the Ce–O distances and thereby enhances the tetragonal crystal field [94]. Of relevance here, the results reported in this thesis have revealed that the symmetric A_{1g} compression (stretching) and symmetric E_g bending of CeO_8 [Figure 2.5(b-c)] are mainly related to the phonon modes in the high-frequency region for garnet structured materials [1, 81]. The activation of these modes induces "dynamical" tetragonal distortions of CeO_8, which most likely accounts for the red-shift of the Ce^{3+} $5d_1 \rightarrow 4f$ emission observed upon increasing temperature.

To summarize, a small modification of the "static" and "dynamical" coordination symmetry of the Ce^{3+} ion sites through cation substitution and/or thermal activation of certain phonon modes are shown to give a significant change in the PL colors of the Ce^{3+} $4f$–$5d$ transitions.

2.2.5 Luminescence intensity

The luminescence intensity is governed by the decay time of the emission τ and the absorption cross section σ of the Ce^{3+} $4f$–$5d$ transitions. τ is defined as the inverse of the spontaneous emission probability, *i.e.* the probability of the $5d_1 \rightarrow 4f$ transitions, which determines the number of the electrons at the excited $5d_1$ level of Ce^{3+} ions at time t that is proportional to $\exp^{-t/\tau}$ [24]. Crucially, the decay time is strongly temperature dependent and depends on both radiative and nonradiative processes happening at elevated temperatures. In particular, temperature increases may lead to a pronounced decrease of both τ and the emission intensity, as shown for YAG:Ce^{3+} in Figure 2.6(a). σ is determined by the probability of electric dipole (absorption) transitions (the number of absorbed photons), which is dictated by the selection rule on the basis of the parity, spin, and symmetry of the wavefunctions at the initial and final states of the Ce^{3+} $4f$–$5d$ transitions. A forbidden transition leads to a decrease of σ and intensity. This is shown by the example of YAG:Ce^{3+} in Figure 2.6(b); the decrease of the intensity observed at temperatures < 500 K is primarily attributed to a reduction of the absorption strength of the $4f \rightarrow 5d_1$ transition because τ remains nearly constant in this temperature range [Figure 2.6(a)]. In general, the apparent drop in luminescence decay time and intensity with increasing temperature is known as thermal quenching of luminescence. To only focus on the thermal quenching of the $5d \rightarrow 4f$ transitions, the analysis of the temperature dependence of τ provides a better and more accurate interpretation than that of the luminescence intensity due to the additional contribution from the absorption strength. A useful measure in this context is the thermal quenching temperature $T_{80\%}$ that is defined as the temperature at which τ has dropped to 80% of the value at low temperatures, usually ≤ 300 K.

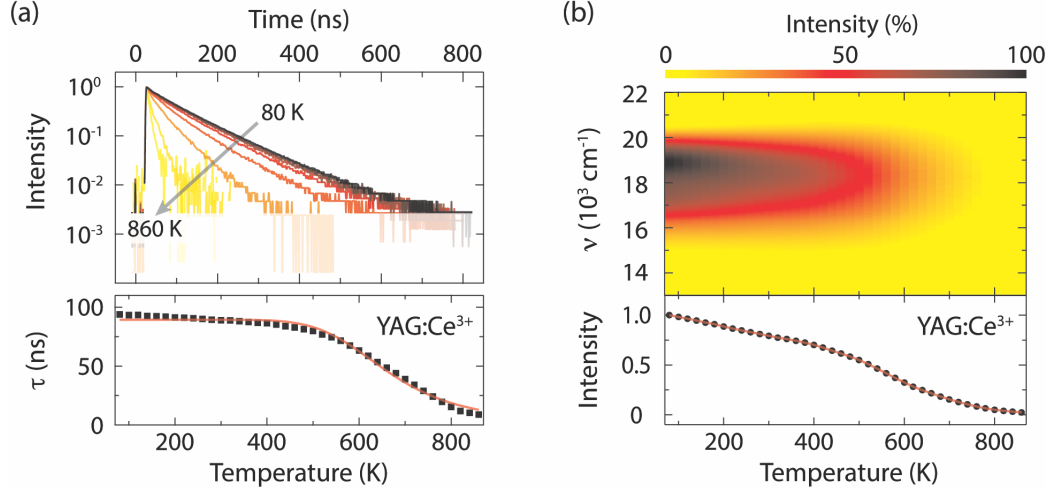Currently, there is a lot of research focusing on understanding the routes

Figure 2.6: Temperature dependence of (a) the decay curves on the top and decay time (τ) at the bottom, and (b) the emission spectra (ν: wavenumber) on the top and normalized emission intensity at the bottom, of YAG:Ce^{3+}, adapted from [14].

of thermal quenching as well as on solutions to suppress them [95–97]. Three major routes have been proposed for Ce^{3+} ions: **1)** nonradiative $5d \rightarrow 4f$ crossover relaxation, **2)** charge trapping at defects through thermal ionization, and **3)** thermally activated concentration quenching.

2.2.5.1   Nonradiative $5d \rightarrow 4f$ crossover relaxation

Nonradiative $5d \rightarrow 4f$ crossover relaxation refers to the process when the excited-state electrons of Ce^{3+} interact with phonons of the host crystal in such a way that the excited-state electrons return to the $4f$ ground state without emitting light. This process may be generally described by a configurational coordinate diagram [98], see Figure 2.7(a). The $4f$ and $5d_1$ electronic configurations of the Ce^{3+} ion in a host are represented by the lower and upper parabolae, respectively. When a sufficient amount of activation energy ΔE [*i.e.* ΔE_1 or ΔE_2 in Figure 2.7(a)] is provided *via* thermal excitation of the vibrational mode(s), the excited-state electrons may reach the crossing point of the $5d_1$ and $4f$ parabolae, which may facilitate the nonradiative return of the $5d_1$ excited state back to the $4f$ ground state through vibrational relaxation.
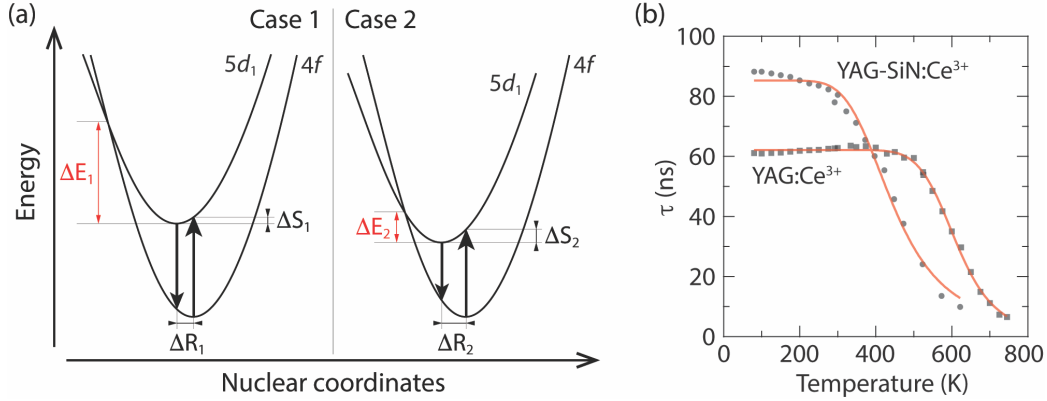
Figure 2.7: (a) Schematic illustration of the nonradiative relaxation through $5d_1 \rightarrow 4f$ crossover for the cases of weak (case 1) and strong (case 2) thermal quenching, following the relations: $|\Delta R_1| < |\Delta R_2|$, $\Delta S_1 < \Delta S_2$, and $\Delta E_1 > \Delta E_2$. Note that the $5d_1$ parabola is generally broader than the $4f$ one because the $5d$ orbital is more spread out than the $4f$ orbital [24]. (b) Decay time τ of YAG:Ce^{3+} ($\lambda_{\mathrm{ex}} = 470$ nm and $\lambda_{\mathrm{em}} = 560$ nm, see Figure 2.4) and YAG:Ce^{3+} co-substituted by Si^{4+}–N^{3-} pairs (YAG-SiN:Ce^{3+}, $\lambda_{\mathrm{ex}} = 520$ nm and $\lambda_{\mathrm{em}} = 750$ nm, see Figure 2.4) as a function of temperature, adapted from [33].

When the $4f$ electron of Ce^{3+} is excited to the $5d_1$ state, the electronic charge distribution of the Ce^{3+} ion becomes more positively charged and Ce^{3+} is thus more attractive to the neighboring O anions. This results in a decrease of the Ce–O bond lengths and lattice relaxation, which shift the $5d$ parabola with respect to the $4f$ parabola by ΔR (< 0) in the nuclear coordinate [99], where $\Delta R = \Delta R_1$ or ΔR_2 in Figure 2.7(a). ΔR may be approximately measured by the difference between the orbital distances for electrons around the nucleus [61], and is often used as a measure of the strength of the electron–phonon coupling, which in turn is usually represented by the so called Huang-Rhys coupling constant S [23, 63, 100, 101]:

$$S = \frac{M\omega^2}{2\hbar\omega}\Delta R^2 \simeq \frac{\Delta S}{2\hbar\omega}. \tag{2.5}$$

Here, M is the effective ionic mass of the moiety related to the vibrational mode in the parabolae, ω is the vibrational frequency of the phonon or local vibrational mode to which the excited-state electron couples, and ΔS is the Stokes shift [$= \Delta S_1$ or ΔS_2 in Figure 2.7(a)]. A larger S means stronger

21

electron–phonon coupling. The comparison between the Case 1 and 2 in Figure 2.7(a) reveals that a larger $|\Delta R|$, which is often reflected by larger ΔS and broader luminescence spectra, gives rise to smaller ΔE [23, 102].

The nonradiative decay rate due to electron–phonon coupling (R_{non}, s^{-1}) is defined as

$$R_{non} = A \cdot \exp^{-\Delta E/kT}, \tag{2.6}$$

where A is the attempt rate of the nonradiative process, k is the Boltzmann constant and T is the temperature [62, 102]. Since the total transition rate from the excited to ground states of Ce^{3+} is $R = R_{rad} + R_{non}$ (R_{rad} is the radiative rate, which is usually independent of temperature), the decay time τ can now be expressed as

$$\tau = \frac{1}{R} = \frac{1}{R_{rad} + A \cdot \exp^{-\Delta E/kT}} . \tag{2.7}$$

The ratio τ/τ_0, where τ_0 is the "intrinsic" decay time (also known as lifetime) without any involvement of nonradiative relaxation, is identical to the quantum efficiency η, which can thus be expressed as

$$\eta = \frac{\tau}{\tau_0} = \frac{1/(R_{rad} + R_{non})}{1/R_{rad}} = \frac{R_{rad}}{R_{rad} + A \cdot \exp^{-\Delta E/kT}} . \tag{2.8}$$

It follows that η and τ are strongly reduced upon increasing T, particularly when $|\Delta R|$ is large and ΔE is small, *cf.* Figure 2.7(a). As an example of enhanced $5d \rightarrow 4f$ crossover relaxation, the incorporation of N^{3-} into the coordination of Ce^{3+} not only lowers the $5d_1$ level but also increases ΔS, which implies a decrease of ΔE [*i.e.* the Case 2 in Figure 2.7(a)]. This gives rise to stronger thermal quenching of luminescence on the Ce^{3+} sites coordinating to N^{3-}, as shown in Figure 2.7(b).

Information about which particular phonon(s) that are at play in thermal quenching processes may be indicated by the phonon side band structure in the luminescence spectra. For instance, high-resolution low-temperature luminescence spectra of YAG:Ce^{3+} have shown a vibronic fine structure with features at around 200 cm^{-1} relative to the zero-phonon line, which suggests that the phonons of energies $\approx$ 200 cm^{-1} may interact with the electrons of

Ce^{3+} ions during the absorption/excitation and emission processes [71, 73].

2.2.5.2 Charge trapping at defects through thermal ionization

Thermal ionization refers to the thermal promotion of electrons of the Ce^{3+} ions into the conduction band (CB) of the host crystal, followed by charge trapping at defects. This process contributes with a nonradiative rate R_{ion} to the total transition rate R, i.e. $R = R_{\mathrm{rad}} + R_{\mathrm{ion}}$, where $R_{\mathrm{ion}} = A_{\mathrm{ion}} \cdot \exp^{-\Delta E_{\mathrm{ion}}/kT}$ and ΔE_{ion} and A_{ion} are the activation energy and rate coefficient of thermal ionization, respectively [25]. Figure 2.8(a) to the right shows one example of thermal ionization when the electrons at the excited state (e) are thermally promoted to the CB (by providing an energy of ΔE_{ion}), and then get trapped by a defect state that may originate from, e.g., defects, such as substitutional impurity atoms, oxygen vacancies, bound excitons and antisite defects [23,103,104]. The trapped electrons might be thermally released from the defect and promoted back into the CB, which still have a low probability of returning to the emitting state and then yielding radiative transitions. In comparison, Figure 2.8(a) to the left shows the case when the electrons are excited from the ground state (g) to the excited state (e) that is situated in the CB, and the delocalized electrons directly recombine with holes at a recombination center. This process is known as photoionization, which leads to strong or even complete quenching of luminescence [23].

Information about thermal ionization in inorganic phosphors can be obtained from measurements of the temperature dependent photoconductivity [106, 107] and thermoluminescence (TL) [108]. An increased photoconductivity and TL glow intensity as a function of increasing (excitation) temperature are a sign of thermal ionization in the material. As an example, Ce^{3+}-doped $Y_3Al_{5-x}Ga_xO_{12}$ (YAGG:Ce^{3+}) shows a pronounced increase of the photoconductivity with increasing Ga concentration [106]. These results are in good agreement with the so called vacuum referred binding energy (VRBE) diagrams of the series of YAGG:Ce^{3+} phosphors [Figure 2.8(b)], which predict the energy levels of the Ce^{3+} ion with respect to the CB of the YAGG host [64, 109]. Therefore, this mechanism appears to reasonably explain the lower quenching temperature of the luminescence decay
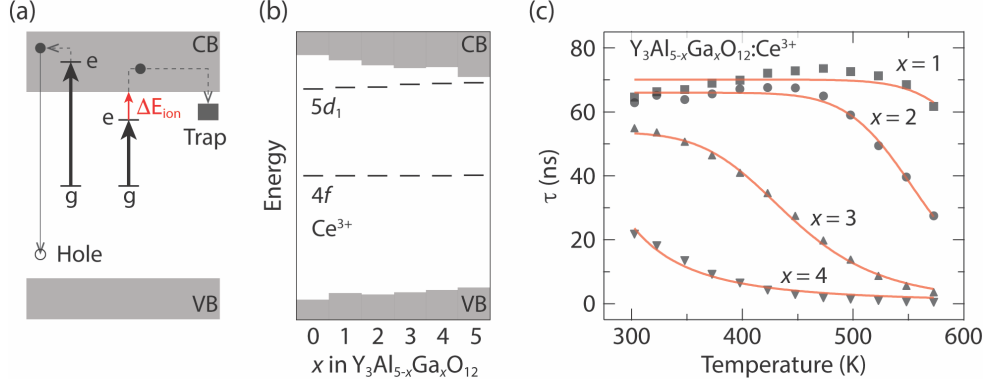
Figure 2.8: (a) Schematic illustration of thermal ionizaion at the luminescent center with the electronic e and g states, for the cases when the e state is situated (*right*) below the CB, and (*left*) within the CB. (b) The VRBE diagrams of $Y_3Al_{5-x}Ga_xO_{12}$:Ce^{3+} phosphors, adapted from [64]. (c) Decay time τ of $Y_3Al_{5-x}Ga_xO_{12}$:Ce^{3+} ($x = 1, 2, 3$, and 4) as a function of temperature, adapted from [105].

time of YAGG:Ce^{3+} upon increasing the Ga substitution [Figure 2.8(c)] and compared to YAG:Ce^{3+} [105, 110, 111]. A similar Ga substitution effect on thermal ionization is also observed in the Ce^{3+}-doped $Y_3Sc_2Al_{3-x}Ga_xO_{12}$ and $Gd_3Al_{5-x}Ga_xO_{12}$ garnet phosphors [52, 53, 105, 112]. A recent study has shown that the quenching temperature of the luminescence decay time of Ce^{3+}-doped $Gd_3Ga_5O_{12}$ is upward-shifted upon increasing pressure, which is attributed to the increase of the energy difference between the Ce^{3+} $5d_1$ level and the CB, *i.e.* to a reduction of thermal ionization. Although the existence of thermal ionization has been well acknowledged thanks to bandgap engineering studies, only few have reported its effect on the reduction of the luminescence decay time on a quantitative scale, which is necessary for an understanding of its competition with other quenching mechanisms. For instance, the thermal quenching of the $5d_1$–$4f$ luminescence of Pr^{3+} in $Y_3Al_{5-x}Ga_xO_{12}$ has been demonstrated to be the result of $5d_1 \rightarrow 4f$ crossover relaxation for $x =$ 0, 1, and 2, whereas of thermal ionization for $x =$ 3, 4, and 5 [113].

2.2.5.3 Thermally activated concentration quenching

Thermally activated concentration quenching refers to thermally enhanced nonradiative energy migration (that is the same as resonance transfer of
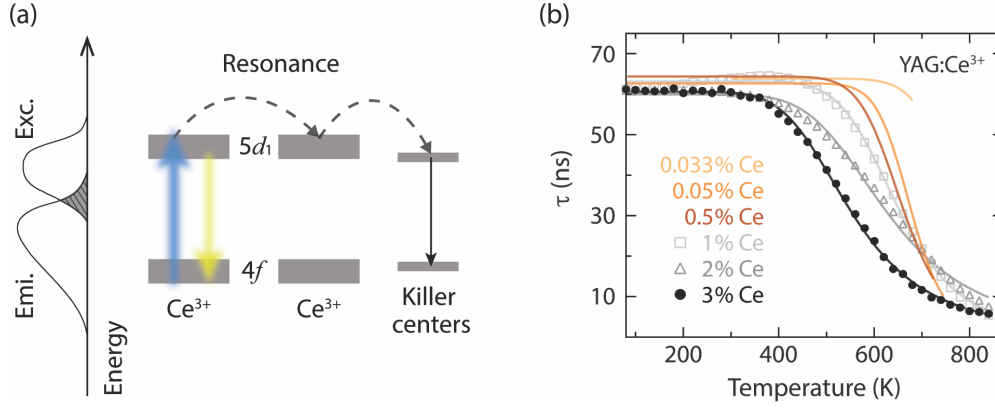
(a)

(b)

Figure 2.9: (a) Illustatrion of thermally activated concentration quenching by nonradiative energy migration among Ce^{3+} ions to luminescence killer centers. The shaded grey area marks the overlap between the excitation (Exc.) and emission (Emi.) spectra, which dictates the probability of resonance transfer of excitation energy between neighboring Ce^{3+} ions. (b) Decay time τ of YAG:Ce^{3+} (with 0.033%, 0.05%, 0.5%, 1%, 2%, and 3% Ce^{3+}, respectively) as a function of temperature. The data are reproduced from refs [71, 108, 114, 115].

electronic excitation energy) among Ce^{3+} ions to luminescence killer centers [25, 71, 116], as depicted in Figure 2.9(a). The nonradiative energy migration is enhanced when the overlap integral of the normalized shape functions of the excitation (or absorption) and emission spectra increases. This may result from the increased energy distribution of the emitting ($5d_1$) level with increasing the Ce^{3+} concentration [1]. More specifically, the increase of the Ce^{3+} concentration tends to yield more lower energy sites for Ce^{3+} (i.e. redshift) due to the enhanced tetragonal distortion of CeO_8, which causes the inhomogeneity of the local environments for the Ce^{3+} ions and hence widens the energy distribution of the Ce^{3+} $4f$–$5d$ transitions. This effect is expected to become more pronounced with elevating temperature due to the increased population of the vibrational levels, i.e. thermal broadening [63]. The energy migration increases the probability of the (excitation) energy trapping at defect sites, such as nonluminescent substitutional impurity atoms, oxygen vacancies, and pairs of the activator ions [24, 116]. This mechanism may be evident from the significant decrease of the quenching temperature of the luminescence decay time of YAG:Ce^{3+} upon increasing Ce^{3+} concentration

[Figure 2.9(b)]. Although the Ce^{3+} doping has shown a clear effect on the thermal stability of the luminescence decay time and intensity, the correlation between thermally activated concentration quenching and the overall quenching behavior is still not fully understood.

2.2.6 Vibrational dynamics

The nature of vibrational dynamics in a crystalline material is dictated by the masses and bond strength of the atoms involved in the vibration, as well as the symmetry properties of the crystal. A garnet crystal, $A_3B_2C_3O_{12}$, is generally characterized by a total of 240 vibrational modes at the Γ-point in the Brillouin zone. These vibrational modes can be expressed using so called irreducible representations as [40]

$$\begin{aligned}
\Gamma = 5A_{1u} + 3A_{1g} + 5A_{2u} + 5A_{2g} + 10E_u + 8E_g + \\
14T_{1g} + 18T_{1u} + 14T_{2g} + 16T_{2u},
\end{aligned} \tag{2.9}$$

where $3A_{1g} + 8E_g + 14T_{2g}$ and $17T_{1u}$ are Raman- and IR-active modes, respectively, $1T_{1u}$ is an acoustic mode, whereas the remaining modes are optically silent ones. These vibrational modes in this case can be described by specific symmetry properties, which stem from the symmetries of the local AO_8, BO_6, and CO_4 moieties and their crystallographic sites in the garnet crystal [117–119]. The vibrational properties such as oscillation direction, frequency, and amplitude of atomic motion are related to the symmetry properties of the mode. Studies of the rare-earth aluminate garnets (A = RE, B = Al, C = Al) have revealed that the lattice vibrations are predominantly related to the displacements of RE atoms in the low frequency range (< 350 cm^{-1}), and to the intramolecular vibrations of AlO_6 and AlO_4 moieties with strong O displacements in the medium-to-high frequency range (350–900 cm^{-1}) [1, 40, 120–122], as reflected by the partial vibrational density of states (DOS) shown in Figure 2.10(a). The vibrational properties may be modified upon varying the chemical composition of the crystal due to the changes of atomic masses, bond lengths, and bond strength on the different crystallographic positions.

Effects of varying A site cations. The series of (Y, Tb, Gd, Lu)$_3$Al$_5$O$_{12}$
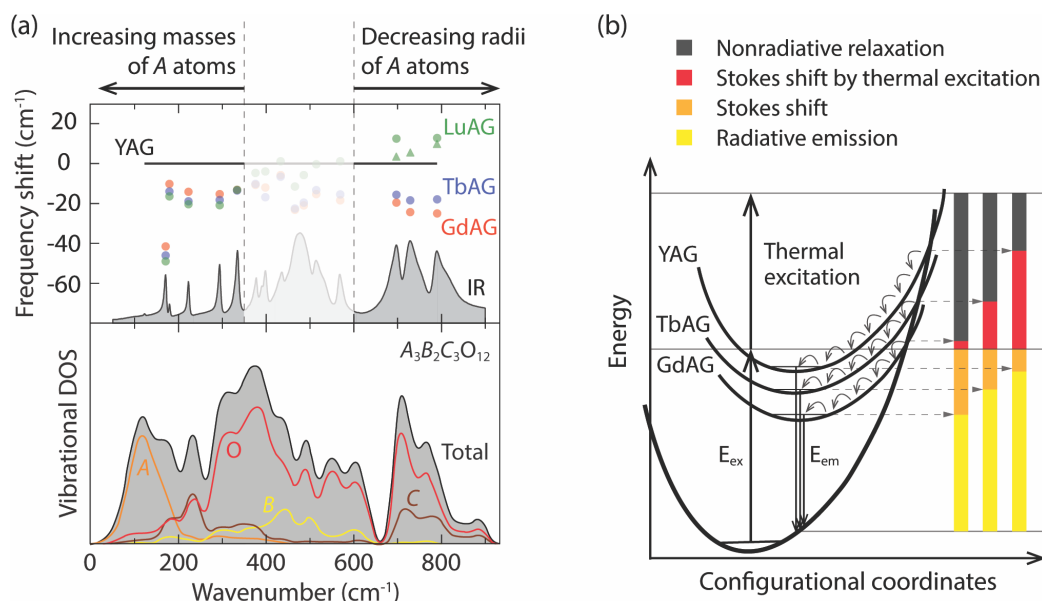
Figure 2.10: (a) *Top*: Frequency shift of the IR modes of LuAG ($Lu_3Al_5O_{12}$), TbAG ($Tb_3Al_5O_{12}$), and GdAG ($Gd_3Al_5O_{12}$), with respect to that of YAG, adapted from [1]. *Bottom*: the partial vibrational DOS of the $A_3B_2C_3O_{12}$ garnet (A is a rare-earth element, and B and C are Al), adapted from [122]. (b) Illustration of the ground- and excited-state configurations of Ce^{3+}-doped YAG, TbAG, and GdAG, shown in configurational coordinate diagrams [49].

garnet crystals shows that the vibrational frequencies of the low-frequency modes (< 350 cm^{-1}) are generally downward shifted for heavier mass on the A site [Y^{3+} (89 u) $<$ Gd^{3+} (157 u) $<$ Tb^{3+} (159 u) $<$ Lu^{3+} (175 u)], whereas the high-frequency modes (> 600 cm^{-1}) generally exhibit an upward-shift of frequency for shorter radii of the A caions [Lu^{3+} (1.12 Å) $<$ Y^{3+} (1.16 Å) $<$ Tb^{3+} (1.18 Å) $<$ Gd^{3+} (1.19 Å)] [1], as shown in Figure 2.10(a). A lowering of the vibrational frequency is an indication of structural softening. A softening is usually reflected by broader potential curves in the configurational coordinate diagram [23, 24], and is further reflected by larger atomic displacement parameters of the constituting atoms obtained from, *e.g.*, neutron and/or X-ray scattering data [42]. The substitution of larger cations for the A cations is found to correlate with the lowering of the parabola of the excited state, which leads to the red-shift of the photoluminescence, as evident from the series of the Ce^{3+}-doped (Y, Tb, Gd)$_3Al_5O_{12}$, see Figure 2.10(b) [49].

Local vibrational properties upon phonon excitation. Apart from the variation of the macroscopic vibrational properties, *e.g.* the frequency of long-range vibrations, the changes of the local vibrational dynamics have been also shown to significantly affect the luminescence properties. Since structural distortions of the local CeO_8 moiety mimic the molecular vibrations of CeO_8, the calculated results of the Ce^{3+} $4f$ and $5d$ configurations when CeO_8 is distorted in certain symmetries [Figure 2.5(b-c)] suggest that a red-shift of the $5d_1 \rightarrow 4f$ emission may occur when the phonon modes exhibiting the A_{1g} symmetric stretching and E_g symmetric bending motions of CeO_8 are activated. The A_{1g} stretching motion is an oscillating process of compressing and expanding the Ce–O bonds, which is also known as the breathing mode. The breathing mode may give rise to not only a red-shift (towards more tetragonal crystal field due to the compression) but also to a blue-shift (towards more cubic crystal field due to the expansion) [41]. On the other hand, the (doubly degenerate) E_g bending motion [Figure 2.11(a)] only contributes to the tetragonal distortions during the oscillation, which leads to a red-shift of the emission. It is worth noting that the shifting effect of the emission color may be essentially dependent on the averaged distortions of the vibrational oscillation since the vibrationally induced distortions are a dynamical process.

To measure the magnitude of the dynamic tetragonal distortions resulting from the E_g bending motion, a distortion parameter, which is defined as the ratio of the long to short O–O distances of CeO_8 as denoted by d_l/d_s, see Figure 2.11(a), is used. This distortion parameter is similar to d_{88}/d_{81} used for quantifying structural distortions caused by cation substitution as introduced earlier [Figure 2.5(a)]. d_l and d_s are calculated from the changes of the bond angles of CeO_8 for any phonon mode. For YAG:Ce^{3+}, the strongest E_g bending motion can be found in the medium-to-high frequency range [Figure 2.11(b)]. The enhancement of the tetragonal distortions reaches about a maximum when the highest-frequency mode is thermally excited. In the case of YAG:Ce^{3+}, the Debye temperature has shown to correlate with the temperature at which the red-shifting effect is most pronounced. This result can be generally applied to other Ce^{3+}-doped garnet phosphors due to the fact that the vibrational symmetry relations are intrinsic to the garnet structure.
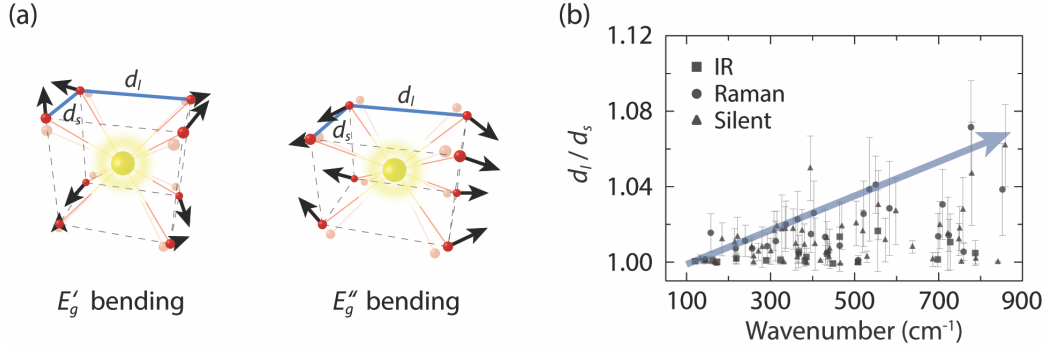
(a)

(b)

Figure 2.11: (a) Illustration of the doubly degenerate E_g bending motions of a cubic CeO_8. (b) Distortion parameter (d_l/d_s) for the E_g bending motions of CeO_8 in YAG:Ce^{3+} for all vibrational modes, adapted from [81].

For YAG:Ce^{3+}, a red-shift of the emission is also observed upon increasing Ce^{3+} concentration, which may be attributed to the systematic downward-shift of the vibrational frequencies of the phonon modes associated with the E_g bending motion of CeO_8 [1]. This means that more vibrational states of these modes are populated at a given temperature, which leads to a greater degree of dynamical tetragonal distortions of CeO_8 and hence a stronger red-shifting effect.

Apart from the color tuning, the excitation of the high frequency phonon modes is found to relate to the thermal quenching of the Ce^{3+}-doped garnet phosphors through the $5d \rightarrow 4f$ crossover relaxation [1, 115]. A comparison between Ce^{3+}-doped $Lu_3Al_5O_{12}$ (LuAG:Ce^{3+}) and $Y_3Al_5O_{12}$ (YAG:Ce^{3+}) phosphors shows that the smaller Lu atoms tend to up-shift the frequencies of the modes in the high-frequency region with respect to that of YAG:Ce^{3+} [Figure 2.10(a)]. In this scenario, the high-frequency modes become less readily activated, which strengthens the structural rigidity and creates the potential to suppress thermal quenching of luminescence. This explains the higher thermal stability of luminescence efficiency for LuAG:Ce^{3+} as compared to YAG:Ce^{3+}. To this end, the vibrational dynamics of inorganic phosphor materials has been shown to significantly influence the color and intensity of the emitted light. However, details of the vibrational effects on these luminescence properties are not fully understood and require further investigations.

Chapter 3

Methodology

To investigate the local structure and vibrational dynamics of garnet type oxide phosphors, I have used a combination of broadband vibrational spectroscopy, mode-selective IR excitation experiments, luminescence experiments, and theoretical and semi-empirical methods. This chapter describes the fundamentals and main characteristics of each technique, especially in regard to the newly performed investigations. For more details about the techniques, the reader is referred to several textbooks, as cited throughout the Chapter.

3.1   Vibrational spectroscopy

The vibrational spectra of materials can be investigated by IR and Raman spectroscopies or by INS, which each of them reveals the energy transitions between vibrational states. In the oversimplified case of a harmonic oscillator, the energy of the vibrational states of a specific mode may be expressed as $E_n \equiv (n + 1/2)h\nu$, where n is the quantum number $(0, 1, 2, ...)$, ν is the vibrational frequency of the mode, and h is the Planck constant. The three techniques rely on different selection rules and, therefore, they are complementary to each other. For instance, vibrational modes that are optically inactive (silent) by photon excitation (*i.e.* by IR and Raman spectroscopies) may be observable in INS. Moreover, IR and Raman spectroscopies only measure zone-center (in the Brillouin zone) modes, whereas INS can probe vibrations at different wavevectors.
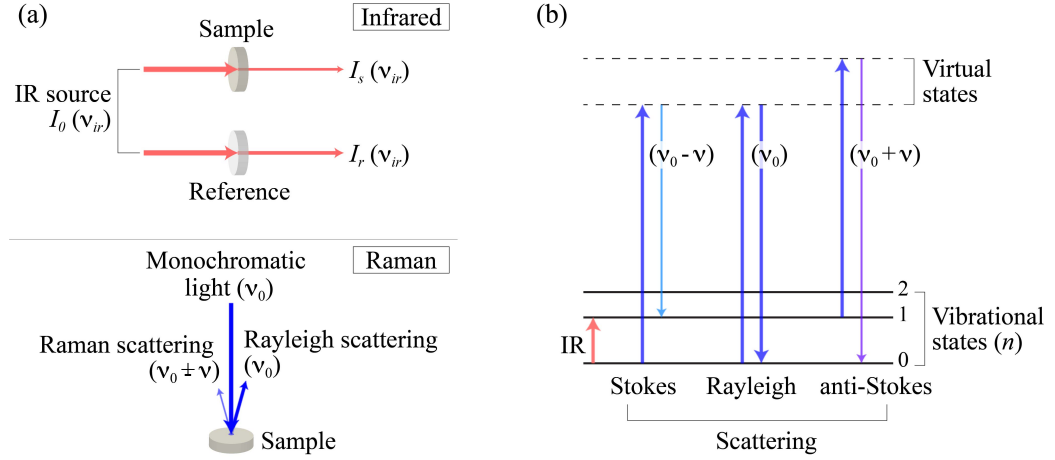
Figure 3.1: (a) Simple scheme for IR and Raman spectroscopies. (b) Energy transition processes for IR- and Raman-active vibrational modes.

Broadband infrared spectroscopy. IR spectroscopy measures the absorption of IR electromagnetic (EM) waves irradiated on a sample. The actual measurement may be performed in either of two different modes of operation, *i.e.* transmittance (absorbance) or reflectance. Figure 3.1(a) shows, as an example, the setup for a typical transmittance (absorbance) measurement, where I_r and I_s are the intensities of the IR light transmitting through the reference and sample, respectively, with a given IR frequency, ν_{ir}. Absorption occurs when the electric dipole moment μ of a molecule oscillates at the identical frequency as that of the oscillating electric field of the incident IR light (*i.e.* at the resonance frequency, $\nu = \nu_{ir}$). It should also meet the condition that the vibration causes a change in μ of the molecule, which is known as the selection rule for IR spectroscopy. The energy of the IR photon is then transferred to the molecule through absorption, which leads to the vibrational transition from, *e.g.*, $n = 0$ to $n = 1$, see Figure 3.1(b). An absorbance-like spectrum can be obtained by taking the logarithm of the reference spectrum divided by the sample spectrum, *i.e.* $\log(I_r/I_s)$.

Broadband Raman spectroscopy. Raman spectroscopy measures the light scattered by the sample as illuminated by monochromatic light of frequency ν_0, see Figure 3.1(a). The oscillating electric field ε [$= \varepsilon_0 \cdot cos(2\pi\nu_0 t)$, where ε_0 is the maximum amplitude of the electric field] of the incident light

induces a dipole moment μ_{ind} (= $\alpha\varepsilon$, where α is the polarizability) in the sample. If α oscillates around the equilibrium polarizability α_0 with the same frequency as that of a specific vibrational mode, *i.e.* $\alpha = \alpha_0 + \Delta\alpha \cdot \cos(2\pi\nu t)$ (where $\Delta\alpha$ is the maximum variation for α), μ_{ind} can be re-formulated as [123]

$$\mu_{ind} = \alpha_0\varepsilon_0\cos(2\pi\nu_0 t) + \frac{1}{2}\Delta\alpha\varepsilon_0\{\cos[2\pi(\nu_0 - \nu)t] + \cos[2\pi(\nu_0 + \nu)t]\}. \quad (3.1)$$

It can be seen that most light is scattered elastically with frequency ν_0, *cf.* the first term in Equation 3.1. This is known as Rayleigh scattering. A small fraction of the light is scattered inelastically with frequency $\nu_0 - \nu$ (Stokes scattering) and $\nu_0 + \nu$ (anti-Stokes scattering), *cf.* the second and third terms in Equation 3.1, respectively. This is known as Raman scattering and occurs when α changes during the vibration. The latter dictates the selection rule for Raman spectroscopy. The elastic and inelastic scattering occurs through the excitation to an intermediate virtual level, where the electronic wavefunctions are temporarily perturbed [119, 124], *cf.* Figure 3.1(b).

Inelastic neutron scattering. INS uses neutrons rather than photons for obtaining a vibrational spectrum. In comparison to IR and Raman spectroscopies, both transferred energy ($\hbar\omega$) and momentum ($\boldsymbol{Q}$) are measured at the same time. The measured quantity is associated with the double differential scattering cross section, $d^2\sigma/(d\Omega dE_f)$, where $d\Omega$ is the solid angle (= A_d/d_f^2, as defined in Figure 3.2), and σ is the total neutron scattering cross section (*i.e.* the number of neutrons scattered in all directions per second divided by the flux of the incident neutrons). The INS intensity is dictated by σ of the constituent atoms and does not rely on any selection rules, which implies that all vibrational modes are in principle measurable. $d^2\sigma/(d\Omega dE_f)$ can be written in terms of coherent and incoherent scattering functions, denoted by $S_{coh}(\boldsymbol{Q}, \omega)$ and $S_{inc}(\boldsymbol{Q}, \omega)$, according to

$$\frac{d^2\sigma}{d\Omega dE_f} = \frac{k_f}{k_i}\frac{\sigma_{coh}}{4\pi}S_{coh}(\boldsymbol{Q}, \omega) + \frac{k_f}{k_i}\frac{\sigma_{inc}}{4\pi}S_{inc}(\boldsymbol{Q}, \omega), \quad (3.2)$$

where $\omega = (E_i - E_f)/\hbar$ for an incident neutron energy of E_i and a final neutron energy of E_f, and σ_{coh} and σ_{inc} are the coherent and incoherent

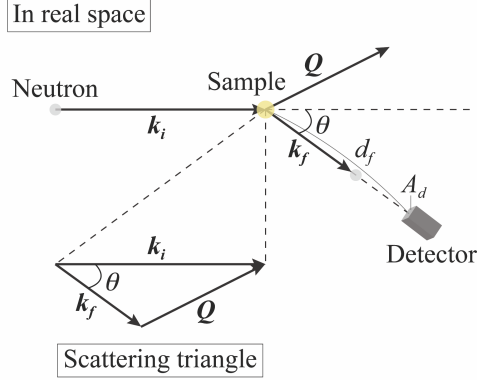Figure 3.2: A scattering process between neutrons and a substance. θ is the scattering angle, $\boldsymbol{k_i}$ and $\boldsymbol{k_f}$ are the wavevectors of the incident and scattered neutrons, respectively, and $\boldsymbol{Q}$ is the transferred momentum (or the scattering vector), adapted from [125].

neutron scattering cross sections, respectively [126, 127]. In a crystal lattice, a local molecular motion (internal mode) is mostly probed by incoherent INS, whereas a collective lattice mode (external mode) is mostly measured by coherent INS [125, 128]. For one specific atom (l), Equation 3.2 can be rewritten as

$$\left(\frac{d^2\sigma}{d\Omega dE_f}\right)_l = \frac{\sigma_l}{4\pi}\frac{k_f}{k_i}\frac{1}{2\pi\hbar}\sum_l \int_{-\infty}^{\infty} dt \langle e^{-i\boldsymbol{Q}\cdot\boldsymbol{r_l}(0)} e^{i\boldsymbol{Q}\cdot\boldsymbol{r_l}(t)} \rangle e^{-i\omega t}, \qquad (3.3)$$

where $\boldsymbol{r_l}(t)$ is the time dependent position vector for the atom l [125]. Equation 3.3 can be further re-formulated in terms of the transition order n (0 for the elastic scattering; 1 for the fundamental transition; 2 for the first overtone, and so forth) and the atomic displacement $\boldsymbol{u}$ of the νth vibrational mode, which is conventionally represented by $S^*(\boldsymbol{Q}, \omega_\nu)$ (related to the amplitude and cross section weighted density of states) as shown in Equation 3.4 [125].

$$S^*(\boldsymbol{Q}, \omega_\nu)_l^n \propto \sigma_l \frac{[(\boldsymbol{Q} \cdot \boldsymbol{u}_{\nu,l})^2]^n}{n!} \exp[-(\boldsymbol{Q} \cdot \sum_\nu \boldsymbol{u}_{\nu,l})^2] \qquad (3.4)$$

The observed intensity in the INS spectrum is proportional to the summation of $S^*(\boldsymbol{Q}, \omega_\nu)_l^n$ over all the atoms in the material.

3.2   Mode-selective infrared excitation experiments

The mode-selective vibrational excitation technique is built on the new generation light source, namely free electron laser (FEL), which provides a high power, tunable, monochromatic, and fast-pulsed IR source over the typical range of lattice vibrations of crystal materials ($\sim$100–1000 cm^{-1}). The IR laser allows to excite one specific IR-active phonon mode at a time, which provides a very powerful means of investigating the effects of a specific phonon involving its local vibrational dynamics on the luminescence properties of inorganic phosphors, as combined with the use of a laser for the PL excitation (Experimental details can be found in Section 4.2). However, the use of the IR laser of high energy flux also gives rise to an heating effect due to the excitation of a specific vibrational mode, which is followed by a fast vibrational relaxation. This in turn leads to an increase of the temperature in the sample. To estimate the temperature increase caused by this effect, a thermal simulation upon the irradiation of the IR laser is performed, which is described as follows.

Two effects are considered in the simulation: **i)** the temperature increase due to the vibrational excitation, and **ii)** the temperature decrease due to the spontaneous dissipation of heat into the surroundings. For the effect **i)**, the variation of the temperature at a specific position in the bulk sample, which is denoted by r, can be calculated using the heat equation as follows [129],

$$\frac{dT}{dt} = \frac{\mathrm{E_{IR}}(r,t)}{Cm}.$$

(3.5)

Here, $\mathrm{E_{IR}}(r,t)$ is the energy of the IR irradiation absorbed by the sample at r per unit time t, which can be calculated using the time dependent spatial distribution of the energy of the IR beam and the IR absorptivity of the sample, and C and m are the heat capacity and mass of the sample, respectively. For the effect **ii)**, the heat dissipation can be regarded as a diffusion process of heat energy driven by the thermal gradients in the sample and between the sample and the surroundings. In this sense, the variation of the temperature can be calculated using the heat equation (originating from

the Fourier's law and the law of energy conservation) as follows [129, 130],

$$\frac{dT}{dt} = \frac{k}{\rho C} \nabla^2 T.$$ (3.6)

Here, k, and ρ are the thermal conductivity, and density of the sample, respectively. By solving the heat equations 3.5 and 3.6, the change in the temperature of the sample upon the IR irradiation over time can be estimated.

3.3 Assignment of vibrational modes

To investigate the vibrational dynamics at and near the activator ions, a novel method has been developed here to systematically assign the local vibrational modes of a crystalline material by using the symmetry properties of the polyhedral moieties (molecules) in the crystal. The assignment of the local modes is expressed by the so called phonon decomposition map (PDM). This section describes the procedures of mapping the extended lattice vibrational modes (phonons) onto a set of localized (molecular) vibrational modes.

3.3.1 Symmetries of molecular vibrations

The basic units of the local vibrational modes in garnet structured crystals are the motions of the dodecahedrally, octahedrally, and tetrahedrally coordinated molecules, which can be categorized into two types. One type refers to intermolecular motions that include translatory and rotary modes. The two modes only spatially move the whole molecules, which means that the molecular symmetries remain the same at any time of vibration. The second type refers to intramolecular motions that involve stretching and bending modes. These can be described in terms of the symmetry coordinates of the molecules $|\eta\rangle$ using the internal coordinates Δs, as follows [123]:

$$|\eta\rangle = \sum_R R \cdot \chi_\eta^R \cdot \Delta s.$$ (3.7)

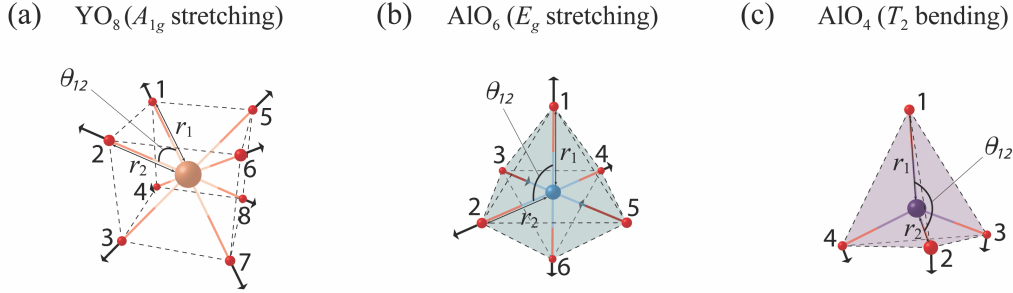(a) YO_8 (A_{1g} stretching)   (b) AlO_6 (E_g stretching)   (c) AlO_4 (T_2 bending)

Figure 3.3: The symmetry coordinates of (a) A_{1g} stretching mode for a cubic YO_8 moiety, (b) E_g stretching mode for an octahedral AlO_6 moiety, and (c) T_2 bending mode for a tetrahedral AlO_4 moiety.

Here χ_η^R is the associated character value (*i.e.* the value corresponding to $|\eta\rangle$ and R in the character table) and Δs is the variation of the internal coordinates (Δr and $\Delta \theta$) prior to employing the symmetry operation R. To graphically illustrate $|\eta\rangle$, Figure 3.3 shows the molecular vibrations of the A_{1g} stretching mode for a cubic YO_8 moiety [131], the doubly degenerate E_g stretching mode for a octahedral AlO_6 moiety [132], and the triply degenerate T_2 bending mode for a tetrahedral AlO_4 moiety [119]. Their symmetry coordinates are shown in Equation 3.8. The full mathematical descriptions of all symmetry coordinates for the three different polyhedral moieties, YO_8, AlO_6, AlO_4, can be found in the supporting information in ref [1].

$$
\begin{aligned}
\text{Figure 3.3(a):} \quad & A_{1g}^r = \Delta(r_1 + r_2 + r_3 + r_4 + r_5 + r_6 + r_7 + r_8) \\
\text{Figure 3.3(b):} \quad & E_g^r = \Delta(r_1 + r_2 - 2r_3 + r_4 - 2r_5 + r_6) \\
\text{Figure 3.3(c):} \quad & T_2^\theta = \Delta(\theta_{12} + \theta_{13} + \theta_{14} - \theta_{23} - \theta_{24} - \theta_{34})
\end{aligned}
\tag{3.8}
$$

The molecules shown in Figure 3.3 are totally symmetric and their point groups are assigned to O_h for the cubic and octahedral molecules and to T_d for the tetrahedral molecule. However, the molecular symmetries are lowered while the molecules are embedded into a crystal lattice, which are thereby assigned by the site symmetries of the crystal lattice. For instance, the site symmetries of YO_8, AlO_6 and AlO_4 molecules in YAG are D_2, S_6 and S_4, respectively. Since lattice vibrations (phonons) are primarily determined by the site symmetry and space group of a crystal, the phonon assignment

with using the symmetry coordinates of totally symmetric molecules is an approximate method for probing the local vibrational symmetries in a crystal lattice.

3.3.2 Assignment of local modes

The PDM provides information of vibrational symmetry and amplitude of all types of local modes for all moieties in the crystal. The key idea of the method is to mathematically project the atomic displacements of a specific moiety of a specific phonon (normal) mode onto the symmetry coordinates which represent different types of local modes. The following description explains the steps to construct a PDM.

From normal modes to atomic displacements. For a crystal containing N atoms in the primitive cell, there are (3N-3) optical and 3 acoustic phonon modes. Generally, the total $3N$ vibrations can be represented by the normal coordinates Q_i, which give the vibrational frequency ν_i and phase δ_i for the ith mode (i = 1, 2, ..., $3N$). The oscillation of all nuclei in a crystal can be expressed by $Q_i = Q_i^0 \sin(2\pi\nu_i t + \delta_i)$, where Q_i^0 is the maximum amplitude of the vibration [119]. Since the 3 acoustic modes exhibit translational motions of the primitive cell as a whole (*i.e.* the center of gravity is stationary), the acoustic modes are not involved in the use of Q_i. In this case, Q_i can be used to represent the (3N-3) normal (vibrational) modes of a N-atom crystal. The Q_i may be transformed into the mass-weighed Cartesian coordinates q_k as

$$q_k = \sum_i B_{ki} Q_i^0 \sin(2\pi\nu_i t + \delta_i), \qquad (3.9)$$

where k stands for one of the x-, y- and z-directions of a cartesian coordinate system, and B_{ki} is a coefficient for the coordination transformation. Physically $q_k = \sqrt{m_k}\Delta V_k$, where m_k is the mass of the nucleus and ΔV_k is the displacement of the nucleus in the direction of k. The correlation between q_k and Q_i (Equation 3.9) reveals that the motion of a nucleus is a superposition of all normal modes [119]. Equation 3.9 also shows that if only a single normal mode, *e.g.* the jth phonon mode ($i = j$), is consid-

ered, all nuclei vibrate in phase with the identical ν_j and δ_j, as expressed by $q_{kj} = B_{kj}Q_j^0\sin(2\pi\nu_j t + \delta_j) = B_{kj}Q_j$. Furthermore, the collective motions of q_{kj} can be correlated to the discrete vibrational levels $[E_{n_j} = (n_j + 1/2)h\nu_j]$ in the quantum mechanics frame by plotting E_{n_j} in a potential parabola with respect to Q_j in a configurational coordinate diagram [Figure 2.1(b)]. The quantum number n_j refers to the number of the jth phonon mode [133]. The eigenvalues (ν_j) and eigenvectors (q_{kj}) can be obtained using DFT calculations [1], lattice dynamics [134], or from a rigid ion model [122]. When analysing local vibrations, the displacement vectors of the nucleus ΔV_k $(= q_k/\sqrt{m_k})$ are used instead of q_k.

From atomic displacements to PDM. Local vibrational modes here refer to molecular vibrations which can be decomposed into translatory, rotary, stretching, and bending modes (Section 3.3.1). The methodology is here exemplified using specific "made-up" examples, including the spectrum, materials, and local motions of molecules, for different steps, as described below.

- Step 1: To extract the atomic displacements of a molecule of interest in the lattice for a particular mode from the calculations, *e.g.* vibration of a H_2O molecule in a cubic lattice for the 20th Raman mode at 692 cm^{-1}, see the Figure below.
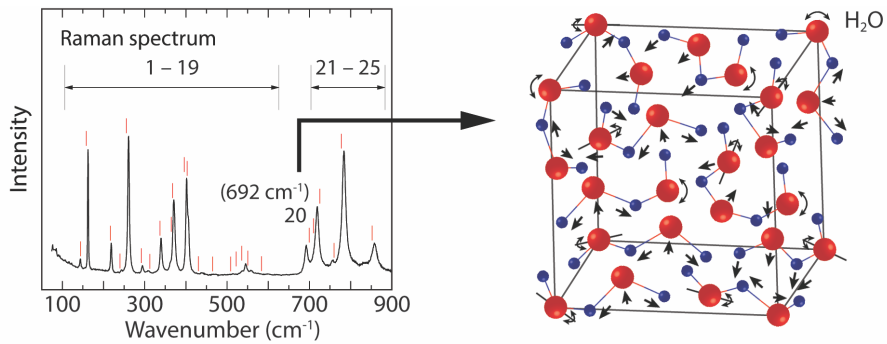
- Step 2: To calculate the direction and displacement of the translatory mode by taking the difference of the center of the molecule between the stationary state and maximum vibration. The calculated translatory mode

is then subtracted from the original molecular vibration, *e.g.* two units of translational vibration in the x-direction are subtracted for the H_2O molecule, see the Figure to the left below.
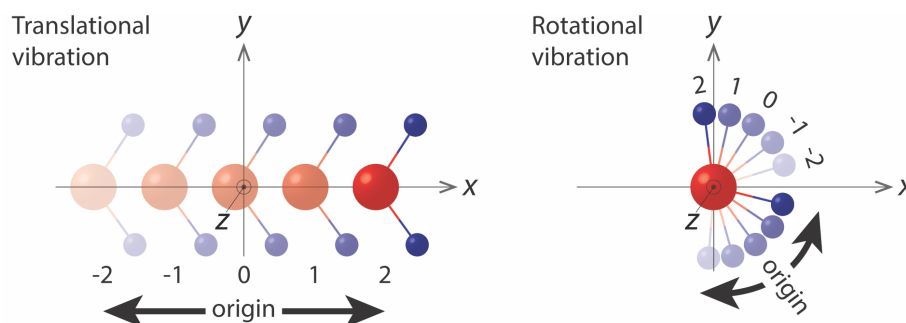
- Step 3: To estimate the rotational axis and angle of the rotary mode by a computationally iterative process. The stationary molecule is rotated about a variable axis by a variable angle with a set boundary condition. The best match between the rotated molecule and the one after subtracting the translatory mode, which needs to fulfil a set criteria, determines the axis and angle. The estimated rotary mode is then subtracted, *e.g.* two units of rotational vibration about the z-axis are subtracted for the H_2O molecule, see the Figure to the right above.

To this point, the "left" molecular vibration comprises only the stretching and bending modes, which is the result of a linear combination of the symmetry coordinates (Section 3.3.1). This linear relation can be expressed as a matrix equation. However, it is noted that the assignments for these two modes are performed separately since they use different internal coordinates.

- Step 4: To estimate the amplitude of the vibrations based on the symmetry coordinates by solving the matrix equation, as shown by the following example. A stretching mode of a tetrahedral moiety is illustrated in the Figure to the left below. The variation of the bond lengths is denoted by Δd_1, Δd_2, Δd_3, and Δd_4, respectively, which equates to a linear sum of the symmetry coordinates A_1, T_2', T_2'', and T_2''' (see Section 3.3.1) with the amplitudes of C_{A_1}, $C_{T_2'}$, $C_{T_2''}$, and $C_{T_2'''}$, respectively. All the symmetry coordinates are normalized to unity and the ones of the triply degenerate

T_2 one are expressed in a way so that they are orthogonal to each other. The amplitudes are simultaneously obtained by solving the matrix equation shown in the Figure to the right below. The average amplitudes of the A_1 and T_2 stretching modes are C_{A_1} and C_{T_2} $[= \sqrt{(C_{T_2'}^2 + C_{T_2''}^2 + C_{T_2'''}^2)}]$, respectively. By following the same procedure but using the internal coordinates of the bond angles instead, the amplitudes of the bending modes can also be estimated.

- Step 5: To construct the full PDM by repeating the procedures from Step 1 to Step 4 for all phonon modes and the corresponding vibrations of all the molecules in the lattice, as demonstrated in ref. [1].

3.4 Photoluminescence experiments

PL spectroscopic measurements refer to the detection of spontaneous emission of photons of, *e.g.*, inorganic phosphors, when light impinges on a material. The details in regard to the intensity and band shape of excitation and emission spectra have been described in Section 2.1. Excitation spectral measurements are usually performed by detecting the intensity of emission of a specific wavelength as a function of the excitation wavelength [135]. Emission spectral measurements are simply performed by detecting the intensity of emission as a function of the emission wavelength upon excitation at a specific wavelength.

To investigate the time dependent PL of phosphors, pulsed light is used as the excitation source. The light pulses promote electrons of population

density N_0 from the ground to excited states at the optical center. The population evolves with time, t, according to

$$N(t) = N_0 e^{-A_T t}, \tag{3.10}$$

where A_T is the total decay rate, *i.e.* the summation of the radiative and non-radiative rates [136]. The radiation intensity $I(t)$, observed by a photon detector, is proportional to $dN(t)/dt$, *i.e.* $I(t) = I(0)e^{-A_T t}$. Therefore, the luminescence decay time τ $(= 1/A_T)$ can be estimated from the time-dependent emission decay curve.

3.5 Vacuum referred binding energy diagrams

VRBE diagrams refer to an energy scheme of the absolute binding energies relative to the energies of the electron at rest in vacuum in the $4f$ and $5d$ electronic states of all trivalent and divalent lanthanides when they are incorporated into a host material. They can be constructed by using the chemical shift model together with the spectroscopic data obtained from PL measurements [64, 137–140]. As an example, Figure 5.5(b) shows the VRBE diagrams of SYG, as doped with Eu^{2+}, Eu^{3+}, or Ce^{3+}. There are five main steps to build the VRBE diagram for the Ce^{3+} ion in SYG. **Step 1** is to determine the energy levels of the bottom of the conduction band (E_c) and the top of the valence band (E_v) with input of the band gap energy, see arrow 1 in Figure 5.5(b). **Step 2** is to determine the energy level of the Eu^{2+} ion in the $4f$ states using the charge transfer energy of $O^{2-} \rightarrow Eu^{3+}$, which equals to the separation between the level of the Eu^{2+} $4f$ states and E_v, see arrow 2 in Figure 5.5(b). **Step 3** is to determine the energy level of the Eu^{3+} ion in the $4f$ states using the $4f$-electron Coulomb repulsion energy of Eu^{3+}, see arrow 3 in Figure 5.5(b). **Step 4** is to determine the energy level of the Ce^{3+} ion in the $4f$ states using the known energy between the Eu^{3+} $4f$ and Ce^{3+} $4f$ states, see arrow 4 in Figure 5.5(b). **Step 5** is to determine the energy level of the Ce^{3+} ion in the $5d$ states using the excitation energy obtained from spectroscopic measurements, see arrow 5 in Figure 5.5(b). By following these steps, important information such as the energy separation between

the Ce^{3+} $5d_1$ level and E_c can be obtained.

3.6 Thermoluminescence experiments

TL occurs *via* a recombination process of electron-hole pairs when a substance, that previously absorbs energy from light excitation, is thermally stimulated. Energy may be charged into trapping (defect) states by optical excitation. More specifically, light may ionize the substance so that electrons and holes are created respectively in the conduction and valence bands. The carriers (the delocalized electrons and holes) might then get trapped at trapping states within the band gap, see Figure 3.4. The trapping states can result from intrinsic defects, such as lattice imperfections, or from extrinsic defects, such as impurities.

Since the carrier trapping at defects is at a non-equilibrium state, which is energetically metastable, the metastable state leads to an attempt to return to an equilibrium state by the annihilation of the electron-hole pairs, resulting in so-called TL glow. For a typical annihilation process, the trapped electrons are firstly promoted from the defect levels to the CB by coupling with thermally activated phonons. Subsequently, the promoted electrons recombine with the trapped holes at the recombination center. However, the annihilation might not occur if the promoted electrons in the delocalized conduction band are re-trapped by the defects. Consequently, TL glow intensity, which depends on the annihilation rate, is primarily determined by the dynamical process of electron de-trapping, electron re-trapping and electron-hole recombination. In first-order kinetics, it assumes that the effect of electron re-trapping is negligible and the TL intensity can be written as

$$I(t) = -\frac{dn}{dt} = n \cdot s \cdot \exp^{-E/kT} = n \cdot R_{de}, \qquad (3.11)$$

where n is the concentration of the trapped electrons, s is a frequency factor in the order of phonon frequency ($\sim 10^{12}$–10^{14} s^{-1}), E is the energy difference between the CB minimum and the electron trapping level, k is the Boltzmann constant, T is the temperature, and R_{de} is the de-trapping rate for one electron [141]. As T is varied linearly by a constant heating rate β, Equa-
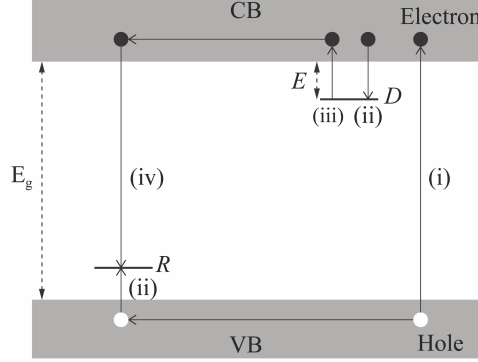
Figure 3.4: Energy band diagram for the one-trap TL model with the steps i) optical excitation, ii) carrier trapping, iii) electron de-trapping, and iv) electron-hole recombination, adapted from [141]. D is the defect, and R is the recombination center.

tion 3.11 can be re-formulated as a function of temperature, see Equation 3.12 [141]. By using the relation $d \ln I(T)/dT = 0$, Equation 3.13 is derived, which reveals that the maximum of TL intensity occurs at the temperature T_m with given values of s, β and E [141]. However, in practice, Equation 3.13 is frequently used for evaluating E instead of T_m.

$$I(T) = -\frac{1}{\beta}\frac{dn}{dt} = n_0 \cdot \frac{s}{\beta} \cdot \exp(-\frac{E}{kT} - \frac{s}{\beta} \cdot \int_{T_0}^{T} \exp^{-E/kT'} dT'), \qquad (3.12)$$

$$\frac{\beta E}{kT_m^2} = s \cdot \exp^{-E/kT_m}, \qquad (3.13)$$

where n_0 and T_0 are n and T at $t = 0$, respectively. Since the intensity of the TL glow curves as a function of temperature is dependent on the excitation temperature (T_{ex}), which is related to the number of charges thermally promoted into the trap states, the distribution of the trap states (or the DOS of the trap) may be determined by the difference between the intensity of the TL glow curves measured at two adjacent T_{ex} [142].

Chapter 4

Instrumentation and details of the experiments

4.1 Vibrational spectroscopy

For the IR spectroscopy measurements reported in this thesis, I used a Fourier transform infrared (FTIR) spectrometer of the model Bruker IFS 66v/s. A key component of a FTIR spectrometer is the interferometer, which contains four major optical elements, a collimating mirror, a beam splitter, a fixed mirror and a moving mirror [Figure 4.1(a)]. The collimating mirror is used to collimate the incoming IR light, which is then partially reflected and transmitted by the beam splitter. The reflected and transmitted IR beams propagate respectively toward the fixed and moving mirrors, which reflect the IR beams back to the beam splitter where they are recombined into one beam. Since the traveling distance is fixed for the beam propagating between the beam splitter and the fix mirror but not for the beam traveling to the moving mirror, the reflected and transmitted beams travel with an optical path difference, δ. This results in an interference pattern, also known as an interferogram. The interferogram is manifested by a combination of constructive and destructive interference. The interference depends on δ and the wavelength (λ) of the IR light, and it is recorded as a function of δ. Each λ is transformed into a cosine wave with a Fourier frequency in real space. The Fourier frequency is correlated with the velocity of the moving mirror,
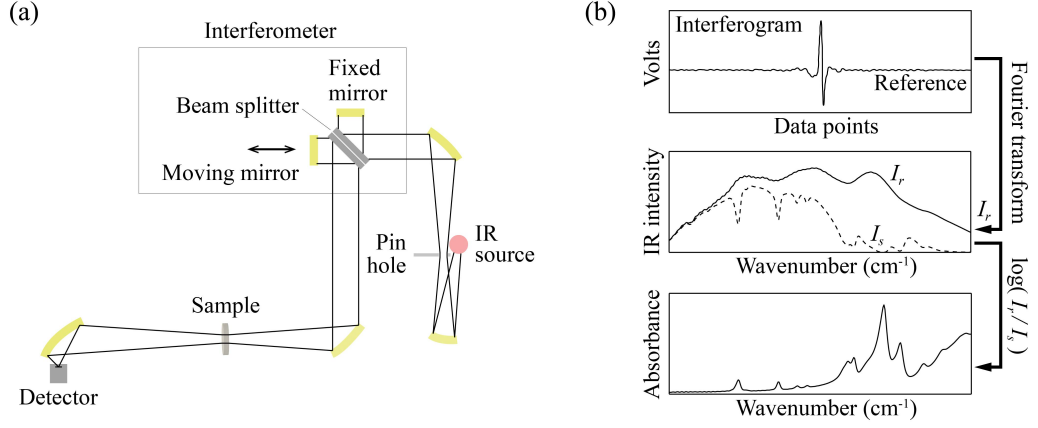
Figure 4.1: (a) Schematic layout of the Bruker IFS 66v/s spectrometer. (b) An interferogram, the transmittance spectra of the reference and sample, and the absorbance spectrum.

and the λ of the IR light [143]. The interferogram shows the summation of all such cosine waves. Therefore, any λ absorption by a sample reduces the amplitude of the interferogram, which is recorded by a detector situated behind the sample. Then, the recorded interferogram is Fourier transformed into a transmittance spectrum [I_r for the reference, or I_s for the sample, as shown in Figure 4.1(b)]. The vibrational spectrum is usually presented as absorbance, *i.e.* $A = \log(I_r/I_s)$, see Figure 4.1(b).

For the Raman spectroscopy measurements performed in this thesis, I used a triple-grating Dilor XY 800 spectrometer. The Dilor XY 800 spectrometer is equipped with a tunable Ar^+/Kr^+ laser, which produces an intense light that is linearly polarized. The linearly polarized light enters a microscope, which focuses the incident beam onto a sample. The backscattered light is guided through the entrance slit, S_1, of the triple grating system, see Figure 4.2. From this point, the optical path depends on the setup of the spectrometer. In this thesis, the so called double subtractive mode was used. In this mode, the polychromatic light coming from the sample is dispersed by the first grating, G_1, and then led to propagate through the second slit, S_2. Here, S_2 acts as a bandpass filter, *i.e.* only light of specific wavelengths can enter the next stage, and thereby the width of S_2 determines the spectral range for detection. In the second stage, the light is merged by the second
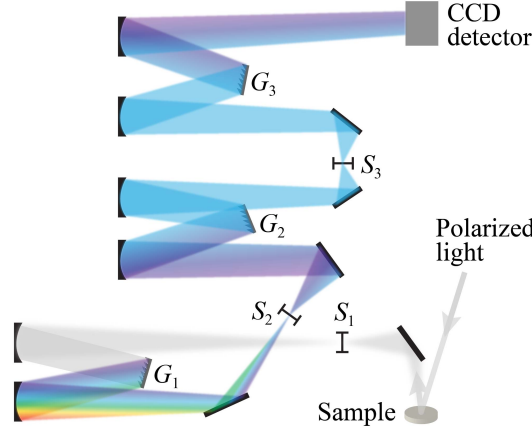
Figure 4.2: Schematic layout of the Dilor XY 800 Raman spectrometer.

grating, G_2, and then focused onto the slit S_3, which rejects stray light. In the third stage, the polychromatic light is dispersed by the third grating G_3 and projected onto a charge-coupled device (CCD) detector cooled by liquid nitrogen. In short, the first and second stages work as a sharp bandpass filter, which significantly reduces stray radiation [144], and thus spectra can be measured close to the laser (Rayleigh) line. The third stage resolves the polychromatic light so that the dispersed light in a wide spectral range can be measured at once by an array detector, *i.e.* the scanning time for a desirable spectral window is shortened.

For the INS spectroscopy measurements performed in this thesis, I used the TOSCA spectrometer as located at the ISIS Pulsed Spallation Neutron and Muon Source at the Rutherford Appleton Laboratory in the U.K. On TOSCA, the sample and analyzer modules are placed in a configuration so that the neutrons are inelastically backscattered by the sample through a constant angle of 45° or 135°, see Figure 4.3. The backscattered neutrons then strike on a graphite crystal analyzer which only allows one wavelength of the neutrons to be Bragg scattered with a given interplanar distance in the crystal [145]. Subsequently, the neutrons pass through a longpass beryllium filter and arrive at the detector. Only neutrons within a narrow energy range can be detected, meaning that the final energy of the neutrons is essentially constant. The difference in energy and momentum, as determined

by time-of-flight, between the incoming and detected neutrons determines the vibrational energy ω_ν and the scattering vector $\boldsymbol{Q}$ (*cf.* Equation 3.4). Since the spectral intensity would be significantly reduced at high temperatures due to thermal motion, which is reflected by $\sum \boldsymbol{u}$ shown in the exponential term (Debye-Waller factor) in Equation 3.4, the measurement is usually performed at < 20 K.
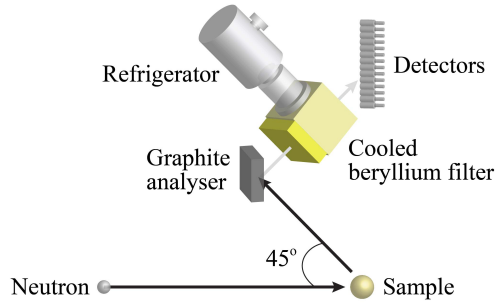

Figure 4.3: The analyzer module of TOSCA, adapted from [145].

4.2 Mode-selective infrared excitation experiments

The most important component for performing the mode-selective infrared excitation experiments is the tunable monochromatic IR source, which can be generated using FELs. The working principle of FELs is described as follows.

Monochromatic light generated by FELs. First, the electrons generated by a electron gun are accelerated by a radio frequency (RF) linear accelerator (linac) to a relativistic speed, *i.e.* close to the speed of light. The electrons are grouped into sub-bunches of ps duration with a repetition rate of the order of GHz, which in turn are encapsulated into bunches of μs duration separated by some hundreds of ms. The bunches are guided into a cavity comprising two highly reflective gold mirrors at the two ends which contain in between an undulator, *i.e.* a series of pairs of permanent magnets with periodically alternating magnetic poles, *cf.* Figure 4.4. The
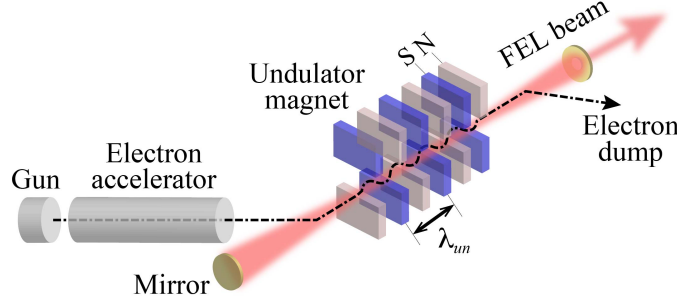
Figure 4.4: Schematic illustration of the working principle of a FEL, adapted from [146].

undulator transversely accelerate electrons so that electrons propagate along the undulator in a zigzag motion, which results in synchrotron radiation due to the radial acceleration of electrons. While the radiation propagates more forwardly by an integer number (n, so called harmonic number [146]) of the radiation wavelength with respect to the electrons, the electrons are in resonance with the radiation. The resonance condition results in a spontaneous emission, which is, however, incoherent radiation. The wavelength of the spontaneous emission λ can be expressed as

$$n\lambda = \frac{\lambda_{un}}{\gamma}\frac{1}{2\gamma}(1 + K^2) = \frac{\lambda_{un}(1 + K^2)}{2\gamma^2},\tag{4.1}$$

where λ_{un} is the periodic distance of the magnetic structure of the undulator, γ is the Lorentz factor ($=1/\sqrt{1-\beta^2}$, $\beta \equiv v/c$, v is the electron velocity and c is the speed of light), and K is a dimensionless parameter which is proportional to the magnetic field B [147, 148].

Since the electric field of the radiation interacts with the oscillating electrons, energy is exchanged between the radiation field and the electrons. The electrons propagate with a faster speed if energy is transferred from the radiation field to the electrons and vice versa. As a result, the forward-drifting electrons from the lagged electron group catch up with the backward-drifting electrons from the advancing electron group. The electrons bunch together periodically on the order of the wavelength of the radiation so that the radiation can be amplified by the coherent spontaneous emission radiated from

(a)

Sample

Filter

Detector   Blue laser

FELIX

Mirror

FEL-2 (3 − 45 μm)   Injector

Linac-2   Linac-1

FEL-1 (30 − 150 μm)

(b) FELIX pulse structure

Micro pulses

100 ms

Macro
pulse

1 ns   ~ps

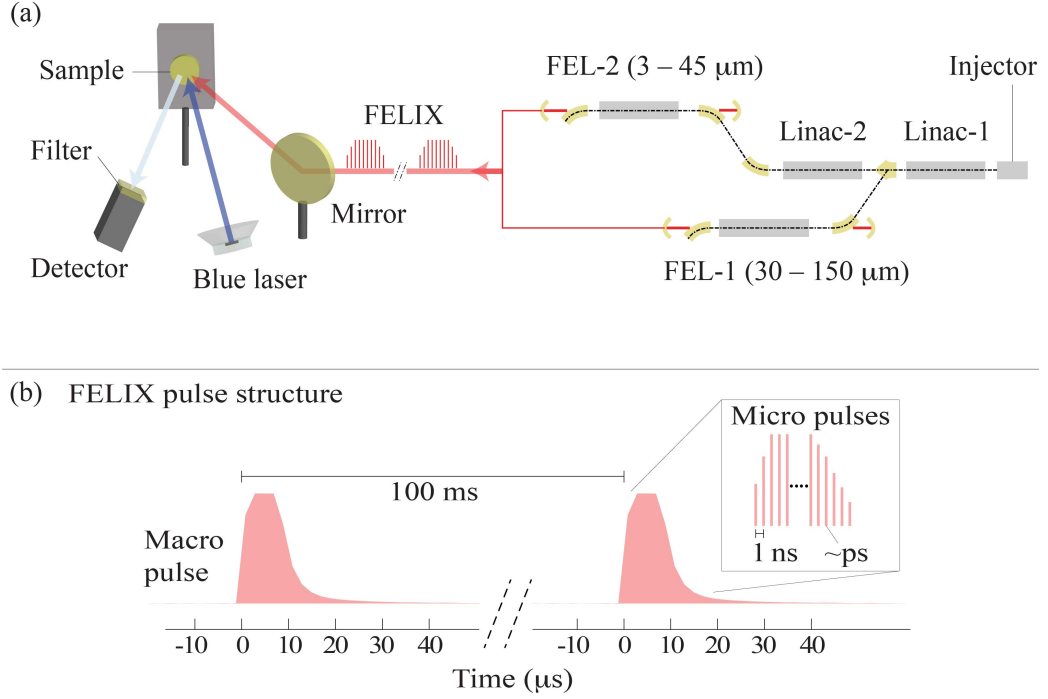-10 0 10 20 30 40   -10 0 10 20 30 40

Time (μs)

Figure 4.5: (a) Schematic layout of FELIX and the setup for the experiments of excitation by FELIX and a blue laser. (b) The pulse structure as generated by FELIX.

the bunched electrons. To acquire an amplification gain, the initial electron velocity is for instance biased by a small forward velocity, which leads to an off-resonance condition, and in this condition the radiation averagely extracts a net energy from the bunched electrons. The off-resonance gain is called the small-signal gain, which enhances the radiation power gradually as the radiation wave cycles in the cavity until the power reaches saturation.

On-site experiments. I used the Free Electron Laser for Infrared eXperiment (FELIX) facility, as located in Nijmegen in the Netherlands. FELIX produces electron pulses of 1 GHz. The pulses are accelerated by linear accelerators (linac-1 and linac-2) to energies of 15–25 and 25–45/50 MeV [149,150], as shown in Figure 4.5(a). The electrons accelerated by linac-1 and linac-2 are guided into two different cavities (FEL-1 and FEL-2), which comprise undulators and two golden mirrors placed at both ends of each cavity. The zig-zag propagation of electrons in the undulators results in spontaneous ra-

diation, which becomes coherent due to energy exchange and stabilization between the radiation and electrons. The radiation is amplified by cycling it in undulators, which is then guided to the user stations.

The radiation wavelength can be modulated by varying the distance between the permanent magnets, *i.e.* adjusting the dimensionless K parameter (the magnetic field **B**), *cf.* Equation 4.1. The IR pulses are tunable in the wavelength ranges of 30–150 μm (333–66 cm^{-1}) for FEL-1 and 3–45 μm (3333–222 cm^{-1}) for FEL-2 [150]. Figure 4.5(b) illustrates the FELIX pulse structure, which consists of macro pulses of 5–10 μs length with a repetition rate of 10 Hz (*i.e.* a cycle period of 100 ms). Each macro pulse is built up of micropulses with a pulse length of *ca.* 1 ps and a repetition rate of 1 GHz, *i.e.* intervals of 1 ns. Each micropulse carries an energy of 1–20 μJ, thus *ca.* 100 mJ for each macropulse [150]. To investigate the thermal quenching mechanism *via* electron–phonon coupling in the Ce^{3+}-doped phosphors (*i.e.* the nonradiative $5d \rightarrow 4f$ crossover relaxation), the sample is simultaneously excited by the FELIX beam (phonon excitation, in 250–1000 cm^{-1}) and a blue pulsed laser (electronic excitation) [see Figure 4.5(a)]. The decay time of the emission from the sample due to the blue excitation is detected as a function of scanning the wavenumber (or wavelength) of the FELIX beam. The variation of the decay time may be the result of the heating effect (Section 3.2) and/or the $5d \rightarrow 4f$ crossover quenching.

4.3 Photoluminescence and thermoluminescence experiments

For the PL and TL measurements, I used a home-built optical setup, as depicted in Figure 4.6(a). The PL spectroscopy measurements rely on a continuous-wave (CW) source for excitation, whereas the measurements of PL decay curves need a pulsed source. To collect the emission spectrum, a commercial spectrometer (Ocean optics USB2000+) working in the ultraviolet and visible (UV-VIS) regions was utilized (with an optical filter). The most critical component of the spectrometer is the grating, which diffracts the light toward a focusing mirror that projects it onto a CCD detector
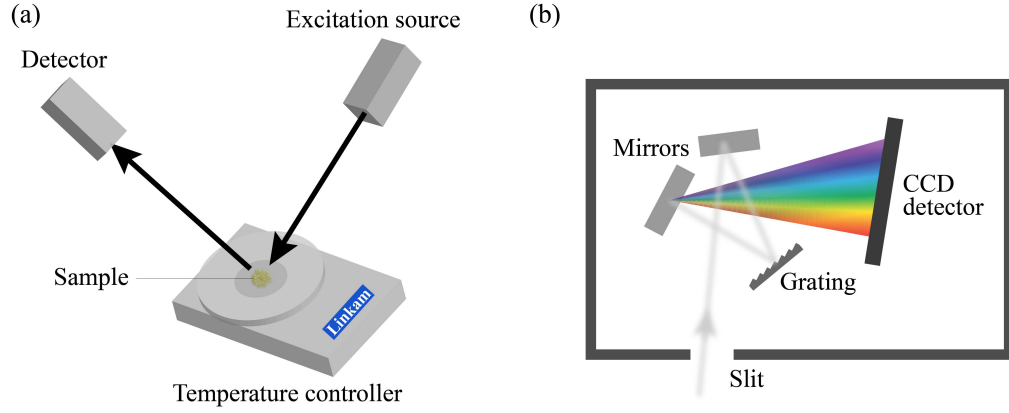
Figure 4.6: Schematic layouts of (a) the optical setup as used for the PL and TL experiments and (b) the Ocean optics USB2000+ spectrometer, adapted from [151].

[Figure 4.6(b)]. Luminescence decay curves were measured by a fast photon detector (Hamamatsu H10721-20) when the sample is excited by pulsed light.

For the TL measurements, the sample was firstly illuminated by an excitation source at a charging temperature for a certain time period. Thereafter, it was rapidly cooled (*e.g.* 100 K/min) down to a low temperature (*e.g.* 300 K, which was the initial temperature before it increased to the charging temperature) to trap the charges at defect states. Upon increasing the temperature with a constant heating rate, the TL glow curve was measured by a photosensor (Hamamatsu H10721-20). The temperature was manipulated by a heating/cooling stage (Linkam THMS600).

Chapter 5

Summary of results and conclusions

As mentioned earlier, the work in this thesis has focused on studying the impact of vibrational dynamics on the luminescence properties of the three Ce^{3+}-doped garnet phosphors YAG:Ce^{3+}, CSS:Ce^{3+}, and SYG:Ce^{3+}. The aim of this Chapter is to summarize and conclude the main findings from this work, as well as their implications for the future.

As a first aspect of the thesis, the host composition dependent photoluminescence color of the $4f$–$5d$ transitions of the Ce^{3+} ions in the YAG, CSS, and SYG hosts was studied by performing UV-VIS spectroscopic measurements. As an example of the results, Figure 5.1(a) shows the $4f$–$5d_1$ excitation and emission spectra of YAG:Ce^{3+}, CSS:Ce^{3+}, and SYG:Ce^{3+}. The excitation spectra show the maxima at around 440 nm for CSS:Ce^{3+}, 427 nm for SYG:Ce^{3+}, and 470 nm for YAG:Ce^{3+}. All bands are located within the emission band of an InGaN blue LED peaking at $\approx$450 nm. The high extent of the spectral overlap between the excitation bands of YAG:Ce^{3+} and CSS:Ce^{3+} and the InGaN blue emission band suggests that they have high QEs of the conversion of blue light into green-yellow light. The smaller bands located at 285 nm for CSS:Ce^{3+}, 297 nm for SYG:Ce^{3+}, and 340 nm for YAG:Ce^{3+} are related to $4f \rightarrow 5d_2$ transitions of Ce^{3+}. A comparison between the energy difference between the band maxima of the excitation transitions to the $5d_2$ and $5d_1$ levels [Figure 5.1(a)] for the three materi-
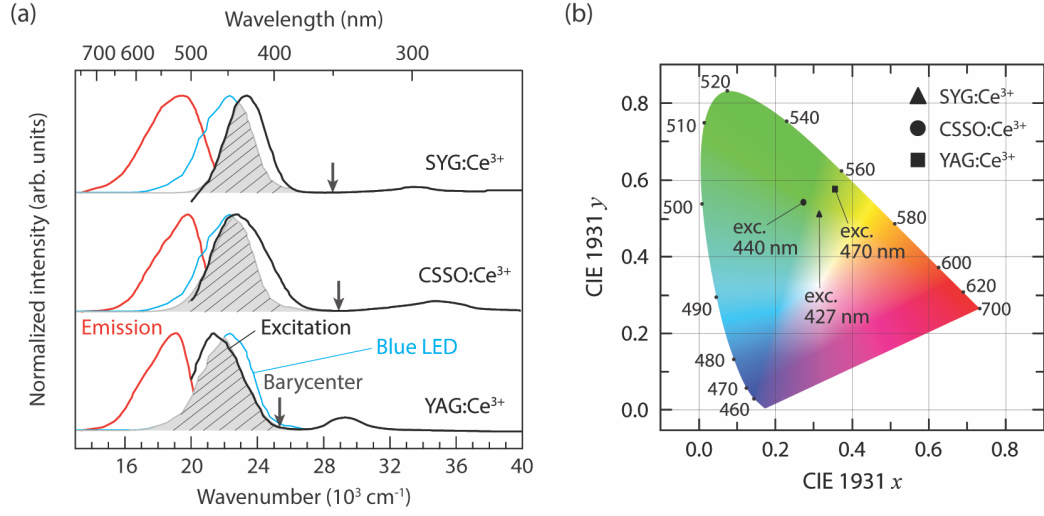
53

Figure 5.1: (a) PL excitation (black color) and emission (red color) spectra of YAG:Ce^{3+}, CSS:Ce^{3+}, and SYG:Ce^{3+}, at RT. The arrows indicate the ^2E_g barycenter of the Ce^{3+} $5d$ levels. (b) CIE 1931 color coordinate diagram for SYG:Ce^{3+}, CSS:Ce^{3+} and YAG:Ce^{3+}, at RT. Figures are modified from **Paper III**.

als reveals that the strength of tetragonal crystal field splitting of the 8-fold coordinated Ce^{3+} ions is stronger in the CSS and SYG hosts compared to YAG. This is in a good agreement with the degree of tetragonal distortions of the CeO$_8$ moieties in the respective hosts, which is estimated using the distortion parameter d_{88}/d_{81} calculated from the respective crystallographic data. The $5d_1 \rightarrow 4f$ emission spectra measured upon excitation at 440 nm (CSS:Ce^{3+}), 427 nm (SYG:Ce^{3+}), and 470 nm (YAG:Ce^{3+}) [Figure 5.1(a)] show that the emission color of YAG:Ce^{3+} is in the green-yellow region, whereas it is in the green region for CSS:Ce^{3+} and SYG:Ce^{3+}, see Figure 5.1(b). Although CSS:Ce^{3+} and SYG:Ce^{3+} exhibit larger tetragonal crystal field splitting than YAG:Ce^{3+}, their excitation and emission spectra are generally located at somewhat higher energies, which is attributed to the fact that the ^2E_g barycenters of the lower $5d$ levels of CSS:Ce^{3+} and SYG:Ce^{3+} are at higher energy levels [Figure 5.1(a)]. This may be the result of a smaller ε_c (Figure 2.3) which in turn is associated with a weaker anion polarizability for the CSS and SYG hosts. Together, these results highlight that the local chemical and structural environments around the Ce^{3+} ion and
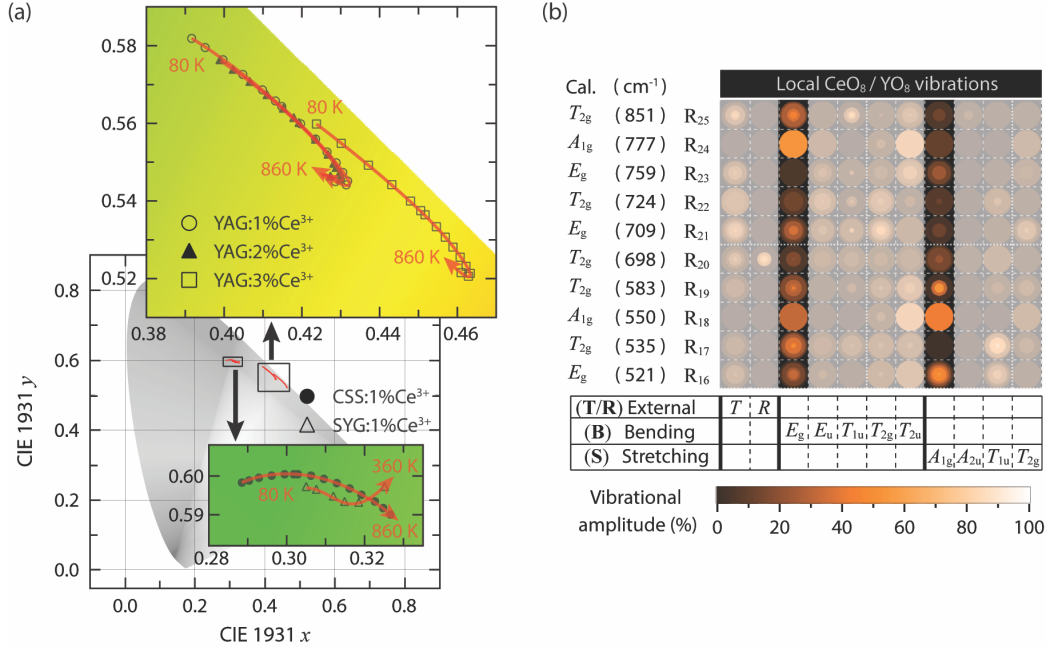
Figure 5.2: (a) Close-up views of the CIE 1931 color coordinate diagram for YAG:x%Ce^{3+} ($x = 1$, 2, and 3), CSS:1%Ce^{3+}, and SYG:1%Ce^{3+}, upon excitation at 454 nm as a function of applied temperature on the respective phosphors. (b) Partial PDM of YAG/YAG:Ce^{3+} highlights the contribution of E_g bending and A_{1g} stretching motions of CeO$_8$/YO$_8$ moieties in the medium-to-high frequency range of the Raman-active modes. Figures are modified from **Paper IV**.

thus the luminescence properties are strongly dependent on the composition of the garnet host.

As a second aspect of this thesis, the $5d_1 \rightarrow 4f$ emission was investigated as a function of garnet host lattice and Ce^{3+} concentration [YAG:x%Ce^{3+} ($x = 1$, 2, and 3), CSS:Ce^{3+}, and SYG:Ce^{3+}] and temperature. Figure 5.2(a) shows that the emission colors of the five studied phosphors are all shifted upon changing temperature. More specifically, the color of YAG:Ce^{3+} exhibits a systematic red-shift upon temperature increase, up to about 740 K, which is followed by a blue-shift upon further temperature increase up to 860 K for all three Ce^{3+} concentrations. A more detailed analysis of the spectra fitted to two Gaussian functions, which correspond to the $5d_1$ to $^2F_{5/2}$ and $^2F_{7/2}$ radiative transitions, shows that the emission bands of YAG:Ce^{3+}

exhibit a similar temperature dependence as the color coordinates for all three Ce^{3+} concentrations, *i.e.* from red-shift to blue-shift upon increasing temperature. Interestingly, the transition temperature of red-to-blue shifting for the $5d_1 \rightarrow {}^2F_{7/2}$ band is observed at around the Debye temperature of YAG:Ce^{3+}, > 500 K, which is lower for higher Ce^{3+} concentrations. This suggests that when the states of the vibrations enhancing tetragonal distortions of the CeO_8 moieties [mainly in the medium-to-high frequency region, see Figure 5.2(b)], are thermally fully populated, a counteracting effect begins to suppress the degree of tetragonal distortions and effectively reverse the optical response. This counteracting effect is attributed to thermal lattice expansion, which turns the local coordination of the CeO_8 moiety into a more cubic symmetry, *i.e.* it weakens the tetragonal crystal field.

For CSS:Ce^{3+} and SYG:Ce^{3+}, the color coordinates exhibit a red-shift up to the highest measurement temperature of T = 860 K (CSS:Ce^{3+}) and T = 360 K (SYG:Ce^{3+}). In detail, the $5d_1 \rightarrow {}^2F_{7/2}$ band of CSS:Ce^{3+} shows a blue-shift upon increasing temperature from 80 to 500 K, whereas a red-shift occurs when the temperature is further increased. This is thus opposed to YAG:Ce^{3+}. In comparison, the $5d_1 \rightarrow {}^2F_{5/2}$ band of CSS:Ce^{3+} generally exhibits a systematic, slight, red-shift with increasing temperature. The opposite effects observed in the $5d_1 \rightarrow {}^2F_{5/2}$ (red-shift) and $5d_1 \rightarrow {}^2F_{7/2}$ (blue-shift) bands imply that the $5d_1 \rightarrow 4f$ transitions may be dictated by a decrease of the strength of the spin-orbit coupling as a function of increasing temperature in the range of 80–500 K. In this context, CSS:Ce^{3+} has a larger Debye temperature based on a simple comparison of the highest frequency of the Raman modes between the YAG and CSS hosts (Figure 5.3). Furthermore, the Raman modes of CSS, which are related to dynamical tetragonal distortions of the CeO_8 moieties, in the range of 800–950 cm^{-1} show a weaker downward shift of frequency upon increasing temperature. This weaker downward shift suggests that CSS:Ce^{3+} is more rigid against an increase of temperature and therefore that it requires more thermal energy for the vibrations to become activated. This is in agreement with the red-shift observed at higher temperatures. For SYG:Ce^{3+}, the relevant Raman modes of the SYG host are found to be in the same frequency range as that of YAG (Figure 5.3). Moreover, they exhibit slightly weaker downward shift of fre-
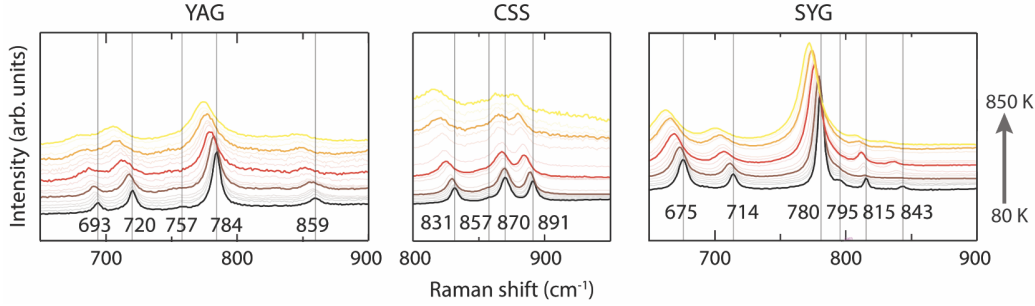
Figure 5.3: Raman spectra of YAG, CSS, and SYG over the temperature range of 80–850 K. Figure is modified from **Paper IV**.

quency as compared to YAG. This implies that SYG:Ce^{3+} would then have a higher transition temperature of red-to-blue shifting than YAG:Ce^{3+}.

In order to quantify the degree of tetragonal distortions of the CeO_8 moieties, which is related to the tetragonal crystal field acting on the Ce^{3+} ion, the distortion parameter d_l/d_s for the E_g bending vibrational modes of CeO_8 moieties [Figure 2.11(a)] may be used. Figure 2.11(b) reveals that strong tetragonal distortions are mainly associated with high-frequency Raman modes (500–900 cm^{-1}) and one optically silent mode at $\sim$400 cm^{-1}. d_l/d_s is increased by as much as $\sim$7% (the effective increase is 3.5% by assuming that the modes exhibit a harmonic oscillation) when the strongest E_g bending vibration of the CeO_8 moiety is fully activated at around Debye temperature. This concurs with an increase of the photon energy of the $5d_1 \rightarrow 4f$ emission maximum by, e.g. $\approx$ 820 cm^{-1} for YAG:1%Ce^{3+}. It follows that the dynamical tetragonal distortions of the CeO_8 moieties have comparable effectiveness on the red-shift of the emission as the static ones that are usually induced by cation substitution on different sites.

As for the lower transition temperature of red-to-blue shifting for higher Ce^{3+} concentrations, this may be attributed to a slight but significant downshift of the three Raman modes R_{17}, R_{24} and R_{25}, which are related to local tetragonal distortions of CeO_8 with increasing Ce^{3+} concentration [Figure 5.2(b)]. Based on a comparison of the frequency of the vibrational modes in different aluminum garnets [Figure 5.4(a)], the frequency downshift of the high frequency vibrational modes (600–900 cm^{-1}) has been associated with the substitution of larger cations on the Y sites in YAG. This explains the ob-
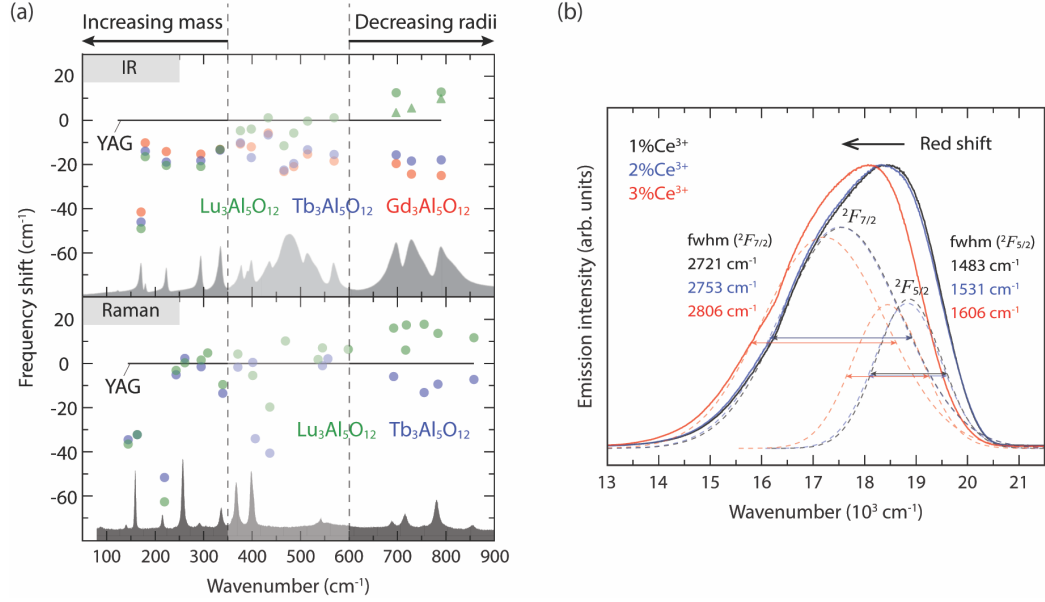
Figure 5.4: (a) Vibrational frequency shifts of IR and Raman modes of aluminum garnets ($RE_3Al_5O_{12}$, RE: rare-earth element) when RE (= Y) is completely substituted by Lu, Tb, or Gd. (b) RT emission spectra of YAG:x%Ce^{3+} (x = 1, 2, and 3). Figures are modified from **Paper II**.

served frequency downshift due to the replacement of Y^{3+} with larger Ce^{3+}.

Apart from the red-shifting effect, the increase of Ce^{3+} concentration in YAG:Ce^{3+} is also found to result in an apparent spectral broadening [Figure 5.4(b)]. The broadening of the emission spectra may be a signature of an increasing energy distribution of the Ce^{3+} $5d$ levels, which may be attributed to increased local structural distortions that make the Ce^{3+} $4f$–$5d$ transition energy less defined due to the increase of the lower energy $5d_1 \rightarrow 4f$ transitions. Therefore, the red-shifted $5d_1 \rightarrow 4f$ emission may originate from an increased probability of radiative energy transfer from higher to lower $5d_1$ levels between Ce^{3+} ions, through reabsorption processes that are primarily determined by the degree of spectral overlap between the excitation and emission spectra. Additionally, a larger Stokes shift is observed for the highest Ce concentrations, suggesting an increased difference of the equilibrated Ce–O distance between the $4f$ ground state and $5d_1$ excited state of Ce^{3+}, *i.e.* similar to the "Case 2" in Figure 2.7(a). This effect may be the result

of an enhanced tetragonal distortion of the CeO_8 moieties, which shortens the equilibrated Ce–O distance when the $4f$ electron is excited into the $5d$ orbital. The increased Stokes shift gives rise to stronger electron–phonon interactions, which in turns broadens the spectra. The observed spectral broadening upon increasing Ce^{3+} concentration is also in agreement with the observed downward-shift of most vibrational modes in YAG:Ce^{3+}, since the lowering in vibrational frequency implies a widening of both the parabolae of the $4f$ ground and $5d_1$ excited state configurations. The widening of the parabolae narrows the distribution between vibrational states within any of the parabolae, meaning that the corresponding vibrational states become more readily populated at a given temperature.

Apart from the significant color shift and/or spectral broadening as established for increasing Ce^{3+} concentration and temperature, the Ce^{3+} concentration and temperature are also shown to impact strongly on the intensity of the emitted light. For YAG:Ce^{3+}, the thermal quenching temperature $T_{80\%}$ decreases from 645 K for 1% Ce^{3+} to 580 K for 3% Ce^{3+}, see Figure 2.9(b). This decrease has been correlated to a downward-shift of the low-frequency modes (< 350 cm^{-1}) due to the larger mass of Ce^{3+}, and of the high-frequency modes (600–900 cm^{-1}) due to the larger radius of Ce^{3+} as compared to that of Y^{3+}, see Figure 5.4(a). The trend of a decreasing vibrational frequency for some specific modes in these frequency ranges would suggest a larger population of these modes at any given temperature. This should increase the probability of electron–phonon interactions that are associated with $5d_1 \rightarrow 4f$ crossover nonradiative relaxation and hence lead to a lowering of $T_{80\%}$. In view of structural rigidity, the substitution of the heavier and larger Ce^{3+} ions for Y^{3+} ions increases the degree of local structural disorder in the YAG crystal, which causes a softening of the material and is manifested as a lowering of the frequency of the vibrational modes. This is perfectly in line with the observed decrease of the Debye temperature of YAG:Ce^{3+} with increasing Ce^{3+} concentration.

Further investigations on the thermal quenching focused on the effect of the garnet host lattice by comparing YAG:Ce^{3+}, CSS:Ce^{3+}, and SYG:Ce^{3+}. The results show that the three phosphors exhibit very different thermal quenching behaviors, see Figure 5.5(a). In the low temperature range (80–
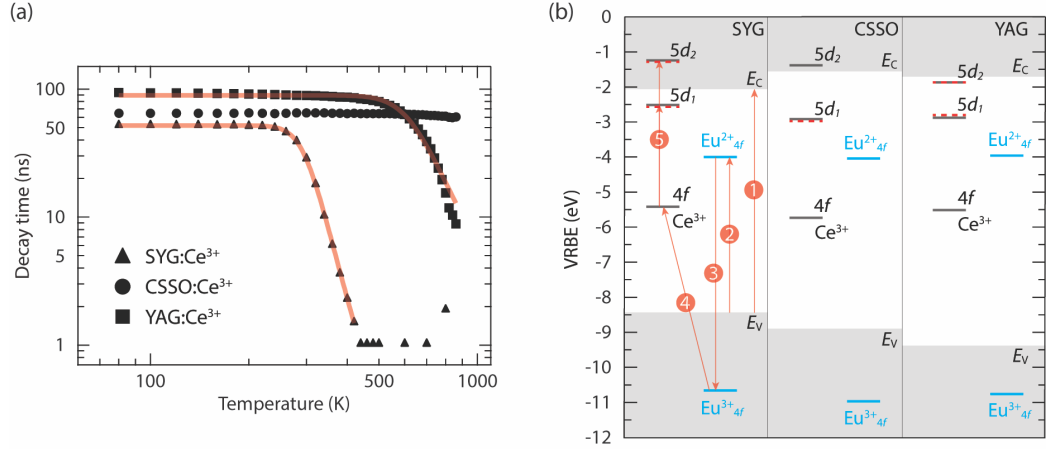
Figure 5.5: (a) Luminescence decay time of SYG:Ce^{3+}, CSS:Ce^{3+}, and SYG:Ce^{3+} as a function of temperature. Red solid curves are fits using a single-barrier quenching model using Equation 2.7. (b) VRBE diagrams for the three hosts, *left*: SYG, *middle*: CSS, and *right*: YAG, as doped with Eu^{2+}, Eu^{3+}, or Ce^{3+}. See Section 3.5 for the details of the arrows 1–5. Figures are modified from **Paper III**.

200 K), the luminescence decay time remains nearly constant for all three phosphors, *i.e.* 52, 65, and 94 ns for SYG:Ce^{3+}, CSS:Ce^{3+}, and YAG:Ce^{3+}, respectively. The onset temperature of thermal quenching (*i.e.* when τ begins to decrease) are observed at approximately 220 K for SYG:Ce^{3+}, 600 K CSS:Ce^{3+}, and 400 K YAG:Ce^{3+}, respectively. Furthermore, the quenching temperatures $T_{80\%}$ are found to be around 280 K for SYG:Ce^{3+}, > 860 K for CSS:Ce^{3+}, and 550 K for YAG:Ce^{3+}. Since the Ce^{3+} concentration is the same in the three phosphors, thermally activated concentration quenching should not be responsible for the significant difference in the thermal quenching temperature between them. This suggests that any of the other two thermal quenching mechanisms (*i.e.* $5d_1 \rightarrow 4f$ crossover relaxation or thermal ionization) are at play. The VRBE diagrams for SYG:Ce^{3+}, CSS:Ce^{3+}, and YAG:Ce^{3+} show that the activation energies of thermal ionization by promoting the Ce^{3+} $5d_1$ electrons into the CB, *i.e.* ΔE_{ion} [*cf.* Figure 2.8(a)], are 0.45 eV (SYG:Ce^{3+}), 1.36 eV (CSS:Ce^{3+}), and 1.17 eV (YAG:Ce^{3+}), see Figure 5.5(b). The trend of increasing the thermal stability of luminescence (*e.g.* higher T$_{80\%}$) with larger ΔE_{ion} would rather suggest

that the thermal quenching behavior is primarily dictated by thermal ionization. However, ΔE_{ion} is found to be generally larger than the activation energy E_a (= 0.33 eV for SYG:Ce^{3+}, 0.5–1.0 eV for CSS:Ce^{3+}, and 0.45 eV for YAG:Ce^{3+}), see Figure 5.5(a), which is associated with the overall behavior of the thermal quenching. The significant difference between ΔE_{ion} and E_a implies that thermal ionization alone cannot dominate the overall quenching behavior, *i.e.* $5d_1 \rightarrow 4f$ crossover relaxation may as well contribute to the overall response of emission intensity upon increasing temperature. Of relevance here, the thermal quenching in YAG:Ce^{3+} has been shown to relate to the excitation of the phonon modes in the frequency range of 600–900 cm^{-1}. For CSS/CSS:Ce^{3+}, the equivalent set of phonon modes is found at higher frequencies (800–900 cm^{-1}, *cf.* Figure 5.3), which means that a higher temperature (more thermal energy) is required for them to be thermally excited. The higher frequencies of these modes may reduce the probability of $5d_1 \rightarrow 4f$ crossover relaxation and thereby increase the thermal stability of τ, *i.e.* higher $T_{80\%}$, for CSS:Ce^{3+}. In comparison, the same set of phonon modes for SYG/SYG:Ce^{3+} is located in the same frequency range as for YAG/YAG:Ce^{3+}, *i.e.* 600–900 cm^{-1}, see Figure 5.3. However, for SYG:Ce^{3+}, $T_{80\%}$ is significantly lower than that for YAG:Ce^{3+}, which implies that thermal ionization strongly dominates the thermal quenching of luminescence in SYG:Ce^{3+}.

Building on these new results, I, together with my colleagues, have also performed a two-laser experiment combining pulsed monochromatized IR light from FELIX together with a pulsed blue laser, with the aim to unveil the effect of coherent large-amplitude excitation of certain IR-active vibrational modes on the luminescence τ of the Ce^{3+} ions in YAG:Ce^{3+}. The results show that τ is overall reduced by several ns upon the irradiation of the IR laser of sufficiently high (flux) energy over the frequency range of 650–860 cm^{-1}, see Figure 5.6(a). Since the sample is heated by the pre-pulse of the IR laser beam prior to the detection of the luminescence decay curves, the variation of τ caused by only this (pre-)heating effect is computationally simulated, as shown by the thick lines in Figure 5.6(a). Note that the heat energy is generated from the fast relaxation of the excited phonons from higher to lower vibrational states. The simulated τ is then subtracted from
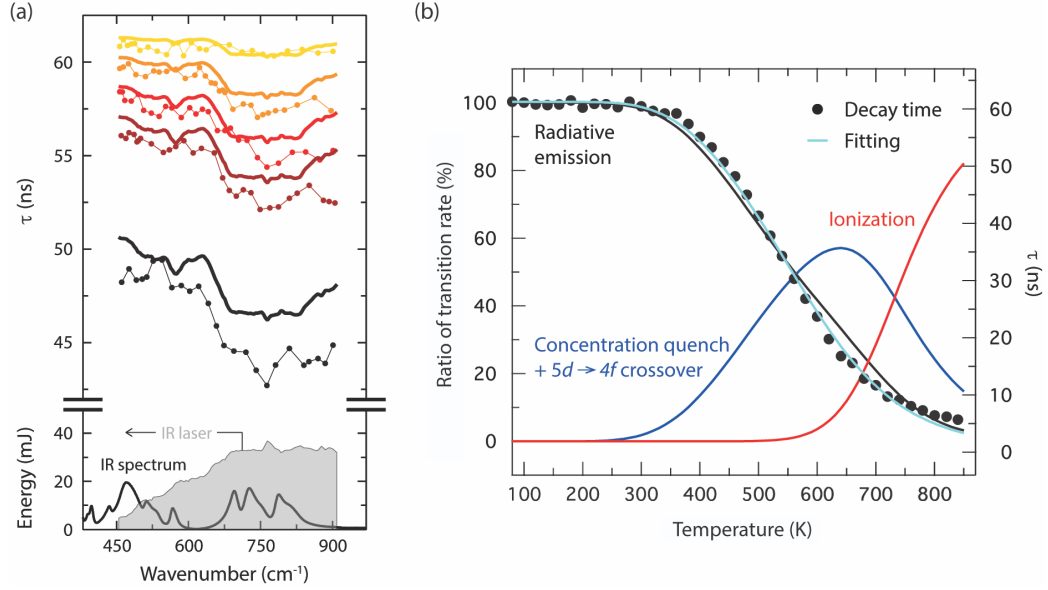
Figure 5.6: (a) *Top*: Experimentally determined luminescence τ for YAG:3%Ce^{3+} upon mode-selective vibrational excitation, measured at 347, 387, 413, 430, and 476 K (applied + local heating) corresponding to the data from upper yellow to lower black dots. The thick lines are the simulated τ, after taking into account the pre-pulse heating by the IR laser. *Bottom*: IR absorbance spectrum of YAG:3%Ce^{3+} (black curve) and the energy flux of the IR laser irradiation (grey area). (b) *Left axis*: ratios of the radiative (black) and nonradiative transition rates that result from thermal ionization (red) and the conbined effect of $5d \to 4f$ crossover relaxation and thermally activated concentration quenching (blue). *Right axis*: τ of YAG:3%Ce^{3+} as well as the fit (turquoise curve) using the single-barrier quenching model (Equation 2.7). Figures are modified from **Paper V**.

the experimentally obtained τ. The value after the subtraction, denoted by $\Delta\tau$, refers to the effect of depopulating the electrons in the emitting $5d_1$ level of Ce^{3+} in a nonradiative manner possibly through $5d_1 \to 4f$ crossover relaxation. The relationship between $\Delta\tau$ and vibrational frequency reveals that the selective excitation of the three highest-frequency IR phonons at 698, 724, and 789 cm^{-1}, which are primarily assigned as different asymmetric bending motions of the CeO$_8$ moieties, may be responsible for the decrease of $\Delta\tau$ *via* the process mentioned above. Furthermore, $\Delta\tau$ is found to progressively increase upon elevating temperature, meaning that the process is temperature

dependent. The average of $\Delta\tau$ over the frequency range of 650–860 cm^{-1} is characterized by an activation energy of 0.23 eV.

Finally, the thermal quenching routes in YAG:Ce^{3+} were investigated with TL glow-curve measurements. The TL results show that three different types of charge-trapping defects are present in YAG:x%Ce^{3+} ($x = 1$, 2, and 3) and that the trap depth (*i.e.* the energy difference between the trapping level and CB) of the three traps is in general similar among different Ce^{3+} concentrations. The fact that the trap depth is virtually independent of the Ce^{3+} concentration suggests that these traps are associated with intrinsic defects of the YAG host lattice. Moreover, the activation energy of filling charges into the deepest trap ($\sim$1.45 eV below the CB) is decreased from E$_{\text{TL}} = 0.29$ eV to E$_{\text{TL}} = 0.15$ eV when increasing the Ce^{3+} concentration from 1% to 3%. This means that charge trapping at this trap occurs more readily and frequently for higher Ce^{3+} concentrations, most likely due to an increased probability of energy migration among Ce^{3+} ions. The significant difference between E$_{\text{ion}}$ [approximately 1 eV, see Figure 5.5(b)] and E$_{\text{TL}}$ suggests that the charge trapping levels are filled directly by athermal tunnelling of charges from the Ce^{3+} 5d_1 level rather than through the CB of the YAG host. This is in line with the broadening of the DOS of this trap upon increasing the Ce^{3+} concentration, which may increase the probability of athermal tunneling processes and hence lower the activation energy. Therefore, the activation energy obtained here (0.29 eV for 1%Ce^{3+} and 0.15 eV for Ce^{3+}) may mimic the activation energy of thermally activated concentration quenching since both processes are assisted by the energy migration among Ce^{3+} ions.

Interestingly, the absolute intensity of the TL glow curves resulting from the deepest trap shows that the TL intensity detected from the 3% Ce^{3+} doped sample is a couple of orders weaker than that from the 1% and 2% Ce^{3+} doped samples. This implies that a relatively large portion of the Ce^{3+} 5d_1 electrons is nonradiatively quenched by another, faster, process, such as 5$d_1 \rightarrow 4f$ crossover relaxation, in the 3% Ce^{3+} sample. This proposition is in agreement with the downward-shift of frequency of several phonon modes in YAG:Ce^{3+} when increasing the Ce^{3+} concentration from 1% to 3%. To this end, the three major thermal quenching processes appear to all contribute to the apparent decrease of τ as a function of temperature increase

in YAG:3%Ce^{3+}. The contribution from each process has been determined by the respective nonradiative transition rate with the input activation energy [Figure 5.6(b)]. It can be concluded that at temperatures below 600 K, the thermal quenching is characterized by both $5d_1 \rightarrow 4f$ crossover relaxation and thermally activated concentration quenching, whereas at > 600 K, thermal ionization is the dominating process.

By bringing together the results from the different studies, this thesis establishes new relationships between the vibrational dynamics and luminescence of garnet type phosphors doped with Ce^{3+}. New Ce^{3+}-doped oxide phosphors emitting at longer wavelengths are shown to require tetragonally distorted environments around the CeO$_8$ moieties and a sufficiently rigid host structure and/or low activator-ion concentration to avoid thermal quenching of luminescence. Moreover, an excellent, intrinsic, thermal stability of luminescence decay time and intensity can be achieved by designing a phosphor compound with a large energy separation between the emitting level of the activator ion and the CB of the host material of the compound, as exemplified by the weak thermal quenching in CSS:Ce^{3+}.

Chapter 6

Prospectives for future work

With a view towards the future, I plan to take on the exciting challenge to investigate the time-resolved structural dynamics of Ce^{3+}-doped garnet phosphors and other similar systems in the transient $5d$ states of Ce^{3+}. The aim is to unveil the parameters, which are significantly important for describing the vibronic state configurations in the configurational coordinate diagram (Figure 2.1), such as the Ce–O bond lengths, structural rigidity, and frequency of the vibrational mode(s) coupled to the excited $5d$ electrons. Slight changes in these parameters have been thought to presumably alter the PL colors and thermal stability of emission intensity, to a large extent, *cf.* Figure 2.7(a). These parameters have been extensively reported in many papers, however, only for materials in the ground states. Hence, further understanding of the structural and vibrational dynamics in the excited state landscape of Ce^{3+} becomes a very critical task.

As a first step in this endeavor, I and my colleagues have performed time-resolved X-ray absorption spectra (TR-XAS) measurements on YAG:Ce^{3+} at the beamline 11-ID-D of the Advanced Photon Source at Argonne National Laboratory, Illinois, United States. The experiments were carried out using a blue pulsed laser as a pumping source to promote the Ce^{3+} $4f$ electron into the $5d$ states, and using synchronized X-ray pulses as a probing source for the Ce L_2-edge absorption. Figure 6.1(a) shows the TR-XAS of YAG:Ce^{3+} in the ground and excited states, respectively. A small but reproducible and significant difference between the two states is observed [Figure 6.1(b)]. These
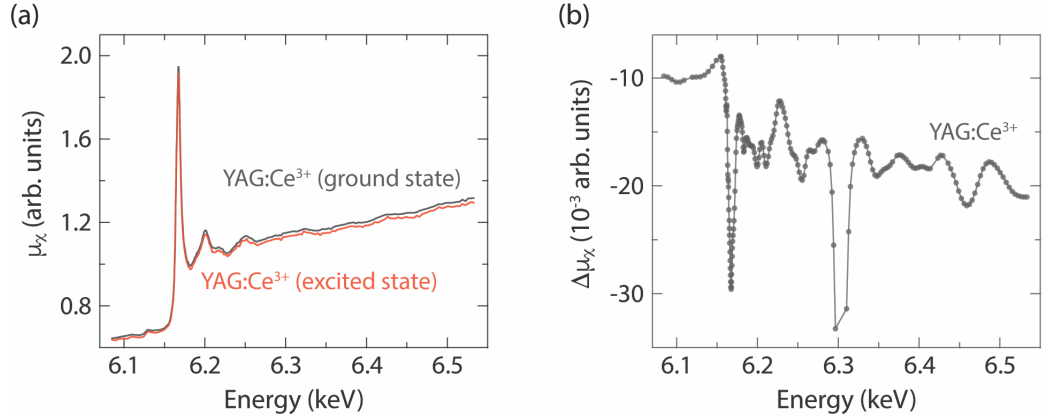
Figure 6.1: (a) Ce L_2-edge TR-XAS of YAG:Ce^{3+} in the $4f$ ground and $5d_1$ excited states. (b) Difference of the Ce L_2-edge TR-XAS spectra of YAG:Ce^{3+} between the ground and excited states.

features are highly interesting and signify changes of the local coordination environments of the Ce^{3+} ion upon the electronic excitation, which are indeed expected to be small according to theoretical predictions [152]. However, to further interpret and fully understand the TR-XAS result, computational modeling using, *e.g.*, DFT calculations is required. In the longer-term, a thorough understanding of the local structural and dynamical properties of YAG:Ce^{3+} can be expected to establish strategies for developing new phosphors with tailored luminescence performance.

Acknowledgments

Bibliography

[1] Yuan-Chih Lin, Paul Erhart, Marco Bettinelli, Nathan C George, Stewart F Parker, and Maths Karlsson. Understanding the interactions between vibrational modes and excited state relaxation in $Y_{3-x}Ce_xAl_5O_{12}$: Design principles for phosphors based on $5d$–$4f$ transitions. *Chemistry of Materials*, 2018.

[2] N Driza, S Blanco-Canosa, M Bakr, S Soltan, M Khalid, L Mustafa, K Kawashima, G Christiani, HU Habermeier, G Khaliullin, et al. Long-range transfer of electron–phonon coupling in oxide superlattices. *Nature Materials*, 11(8):675, 2012.

[3] Matteo Rini, Nicky Dean, Jiro Itatani, Yasuhide Tomioka, Yoshinori Tokura, Robert W Schoenlein, Andrea Cavalleri, et al. Control of the electronic phase of a manganite by mode-selective vibrational excitation. *Nature*, 449(7158):72, 2007.

[4] EJ Spahr, L Wen, M Stavola, LA Boatner, LC Feldman, NH Tolk, and G Lüpke. Giant enhancement of hydrogen transport in rutile TiO_2 at low temperatures. *Physical Review Letters*, 104(20):205901, 2010.

[5] Sarah Maria Falke, Carlo Andrea Rozzi, Daniele Brida, Margherita Maiuri, Michele Amato, Ephraim Sommer, Antonietta De Sio, Angel Rubio, Giulio Cerullo, Elisa Molinari, et al. Coherent ultrafast charge transfer in an organic photovoltaic blend. *Science*, 344(6187):1001–1005, 2014.

[6] Aurelien MA Leguy, Jarvist Moore Frost, Andrew P McMahon, Victoria Garcia Sakai, W Kockelmann, ChunHung Law, Xiaoe Li, Fabrizia Foglia, Aron Walsh, Brian C Oregan, et al. The dynamics of methylammonium ions in hybrid organic–inorganic perovskite solar cells. *Nature communications*, 6:7124, 2015.

[7] Cristian I Contescu, Craig M Brown, Yun Liu, Vinay V Bhat, and Nidia C Gallego. Detection of hydrogen spillover in palladium-modified

activated carbon fibers during hydrogen adsorption. *The Journal of Physical Chemistry C*, 113(14):5886–5890, 2009.

[8] Siddha Pimputkar, James S Speck, Steven P DenBaars, and Shuji Nakamura. Prospects for LED lighting. *Nature Photonics*, 3(4):180–182, 2009.

[9] European Commission. Green Paper - Lighting the Future: Accelerating the deployment of innovative lighting technologies. *Green Paper - Lighting the Future: Accelerating the deployment of innovative lighting technologies*, pages 1–19, 2011.

[10] Shuji Nakamura, Takashi Mukai, and Masayuki Senoh. Candela-class high-brightness InGaN/AlGaN double-heterostructure blue-light-emitting diodes. *Applied Physics Letters*, 64(13):1687–1689, 1994.

[11] Isamu Akasaki, Hiroshi Amano, and Shuji Nakamura. Blue LEDs–Filling the world with new light. *Nobel Prize Lecture. Stockholm: The Nobel Foundation. Available at https://assets.nobelprize.org/uploads/2018/06/popular-physicsprize2014-1.pdf (accessed 26 September 2018)*, 2014.

[12] Roya Mirhosseini, Martin F Schubert, Sameer Chhajed, Jaehee Cho, Jong Kyu Kim, and E Fred Schubert. Improved color rendering and luminous efficacy in phosphor-converted white light-emitting diodes by use of dual-blue emitting active regions. *Optics express*, 17(13):10806–10813, 2009.

[13] Michael R Krames, Oleg B Shchekin, Regina Mueller-Mach, Gerd O Mueller, Ling Zhou, Gerard Harbers, and M George Craford. Status and future of high-power light-emitting diodes for solid-state lighting. *Journal of Display Technology*, 3(2):160–175, 2007.

[14] Suchinder K Sharma, Yuan-Chih Lin, Irene Carrasco, Tobias Tingberg, Marco Bettinelli, and Maths Karlsson. Weak thermal quenching of the luminescence in the $Ca_3Sc_2Si_3O_{12}$:Ce^{3+} garnet phosphor. *Journal of Materials Chemistry C*, 2018.

[15] Ching-Cherng Sun, Yu-Yu Chang, Tsung-Hsun Yang, Te-Yuan Chung, Cheng-Chien Chen, Tsung-Xian Lee, Dun-Ru Li, Chun-Yan Lu, Zi-Yan Ting, Benoît Glorieux, et al. Packaging efficiency in phosphor-converted white leds and its impact to the limit of luminous efficacy. *Journal of Solid State Lighting*, 1(1):19, 2014.

[16] A Setlur. Phosphors for LED-based solid-state lighting. *The Electro-chemical Society Interface*, 16(4):32, 2009.

[17] S Ye, F Xiao, Y X Pan, Y Y Ma, and Q Y Zhang. Phosphors in phosphor-converted white light-emitting diodes: Recent advances in materials, techniques and properties. *Materials Science and Engineering: R: Reports*, 71(1):1–34, 2010.

[18] Philippe F Smet, Anthony B Parmentier, and Dirk Poelman. Selecting conversion phosphors for white light-emitting diodes. *Journal of the Electrochemical Society*, 158(6):R37–R54, 2011.

[19] Chun Che Lin and Ru-Shi Liu. Advances in Phosphors for Light-emitting Diodes. *The Journal of Physical Chemistry Letters*, 2(11):1268–1277, 2011.

[20] Yuan-Chih Lin, Maths Karlsson, and Marco Bettinelli. Inorganic Phosphor Materials for Lighting. *Topics in Current Chemistry*, 374(2):1–47, 2016.

[21] Zhiguo Xia and Quanlin Liu. Progress in discovery and structural design of color conversion phosphors for leds. *Progress in Materials Science*, 84:59 – 117, 2016.

[22] Zhiguo Xia and Andries Meijerink. Ce^{3+}-doped garnet phosphors: composition modification, luminescence properties and applications. *Chemical Society Reviews*, 46:275–299, 2017.

[23] G Blasse and B C Grabmaier. *Luminescent materials*, volume 44. Springer-Verlag Berlin, 1994.

[24] S. Shionoya, W. M. Yen, and H. Yamamoto. *Phosphor Handbook*. CRC Press, 2006.

[25] Baldassare Di Bartolo. *Advances in nonradiative processes in solids*, volume 249. Springer Science & Business Media, 2013.

[26] Yuexiao Pan, Mingmei Wu, and Qiang Su. Tailored photoluminescence of YAG:Ce phosphor through various methods. *Journal of Physics and Chemistry of Solids*, 65(5):845–850, 2004.

[27] Nathan C George, Kristin A Denault, and Ram Seshadri. Phosphors for Solid-State White Lighting. *Annual Review of Materials Research*, 43(1):481–501, 2013.

[28] Won Bin Im, Natalie N Fellows, Steven P DenBaars, Ram Seshadri, and Young-Il Kim. $LaSr_2AlO_5$, a versatile host compound for Ce^{3+}-based yellow phosphors: structural tuning of optical properties and use in solid-state white lighting. *Chemistry of Materials*, 21(13):2957–2966, 2009.

[29] Yasuo Shimomura, Tetsuo Honma, Motoyuki Shigeiwa, Toshio Akai, Kaoru Okamoto, and Naoto Kijima. Photoluminescence and Crystal Structure of Green-Emitting $Ca_3Sc_2Si_3O_{12}$:Ce^{3+} Phosphor for White Light Emitting Diodes. *Journal of The Electrochemical Society*, 154(1):J35–J38, 2007.

[30] Ho Seong Jang, Heesun Yang, Sung Wook Kim, Ji Yeon Han, Sang-Geun Lee, and Duk Young Jeon. White light-emitting diodes with excellent color rendering based on organically capped CdSe quantum dots and Sr_3SiO_5:Ce^{3+}, Li^+ phosphors. *Advanced Materials*, 20(14):2696–2702, 2008.

[31] Ho Seong Jang and Duk Young Jeon. Yellow-emitting Sr_3SiO_5:Ce^{3+}, Li^+ phosphor for white-light-emitting diodes and yellow-light-emitting diodes. *Applied Physics Letters*, 90(4):041906, 2007.

[32] Ali Kalaji, Paul J Saines, Nathan C George, and Anthony K Cheetham. Photoluminescence of cerium-doped $(Ca_{1-x}Sr_x)_3RE_2Ge_3O_{12}$ garnet phosphors for solid state lighting: Relating structure to emission. *Chemical Physics Letters*, 586:91–96, 2013.

[33] Anant A Setlur, William J Heward, Mark E Hannah, and Uwe Happek. Incorporation of Si^{4+}–N^{3-} into Ce^{3+}-doped garnets for warm white LED phosphors. *Chemistry of Materials*, 20(19):6277–6283, 2008.

[34] Kazuki Asami, Jumpei Ueda, Masahiro Shiraiwa, Kotaro Fujii, Masatomo Yashima, and Setsuhisa Tanabe. Redshift and thermal quenching of Ce^{3+} emission in $(Gd, Y)_3(Al, Si)_5(O, N)_{12}$ oxynitride garnet phosphors. *Optical Materials*, 2018.

[35] Yongfu Liu, Xia Zhang, Zhendong Hao, Xiaojun Wang, and Jiahua Zhang. Generation of broadband emission by incorporating N^{3-} into $Ca_3Sc_2Si_3O_{12}$:Ce^{3+} garnet for high rendering white LEDs. *Journal of Materials Chemistry*, 21(17):6354–6358, 2011.

[36] YQ Li, N Hirosaki, RJ Xie, T Takeda, and M Mitomo. Yellow-orange-emitting $CaAlSiN_3$:Ce^{3+} phosphor: structure, photoluminescence, and

application in white leds. *Chemistry of Materials*, 20(21):6704–6714, 2008.

[37] Liangliang Zhang, Jiahua Zhang, Xia Zhang, Zhendong Hao, Haifeng Zhao, and Yongshi Luo. New yellow-emitting nitride phosphor $SrAlSi_4N_7:Ce^{3+}$ and important role of excessive AlN in material synthesis. *ACS applied materials & interfaces*, 5(24):12839–12846, 2013.

[38] Won Bin Im, Nathan George, Joshua Kurzman, Stuart Brinkley, Alexander Mikhailovsky, Jerry Hu, Bradley F Chmelka, Steven P DenBaars, and Ram Seshadri. Efficient and color-tunable oxyfluoride solid solution phosphors for solid-state white lighting. *Advanced Materials*, 23(20):2300–2305, 2011.

[39] S Geller. Crystal chemistry of the garnets. *Zeitschrift für Kristallographie - Crystalline Materials*, 125(1-6):1–47, 1967.

[40] J P Hurrell, S P S Porto, I F Chang, S S Mitra, and R P Bauman. Optical Phonons of Yttrium Aluminum Garnet. *Physical Review*, 173(3):851–856, sep 1968.

[41] Jennifer L Wu, Gautam Gundiah, and A K Cheetham. Structure-property correlations in Ce-doped garnet phosphors for use in solid state lighting. *Chemical Physics Letters*, 441(46):250–254, 2007.

[42] Nathan C George, Andrew J Pell, Géraldine Dantelle, Katharine Page, Anna Llobet, M Balasubramanian, Guido Pintacuda, Bradley F Chmelka, and Ram Seshadri. Local Environments of Dilute Activator Ions in the Solid-State Lighting Phosphor $Y_{3-x}Ce_xAl_5O_{12}$. *Chemistry of Materials*, 25(20):3979–3995, 2013.

[43] T Y Tien, E F Gibbons, R G DeLosh, P J Zacmanidis, D E Smith, and H L Stadler. Ce^{3+} Activated $Y_3Al_5O_{12}$ and Some of Its Solid Solutions. *Journal of The Electrochemical Society*, 120(2):278–281, 1973.

[44] Lucie Devys, Géraldine Dantelle, Geneva Laurita, Estelle Homeyer, Isabelle Gautier-Luneau, Christophe Dujardin, Ram Seshadri, and Thierry Gacoin. A strategy to increase phosphor brightness: Application with Ce^{3+}-doped $Gd_3Sc_2Al_3O_{12}$. *Journal of Luminescence*, 190:62–68, 2017.

[45] Robert D Shannon. Revised effective ionic radii and systematic studies of interatomic distances in halides and chalcogenides. *Acta crystallographica section A: crystal physics, diffraction, theoretical and general crystallography*, 32(5):751–767, 1976.

[46] Yasuo Shimomura, Tomoyuki Kurushima, Motoyuki Shigeiwa, and Naoto Kijima. Redshift of green photoluminescence of $Ca_3Sc_2Si_3O_{12}$:Ce^{3+} phosphor by charge compensatory additives. *Journal of the electrochemical society*, 155(2):J45–J49, 2008.

[47] Paolo Ghigna, Sonia Pin, Cees Ronda, Adolfo Speghini, Fabio Piccinelli, and Marco Bettinelli. Local structure of the Ce^{3+} ion in the yellow emitting phosphor YAG:Ce. *Optical Materials*, 34(1):19–22, 2011.

[48] Lars Vegard. Die konstitution der mischkristalle und die raumfüllung der atome. *Zeitschrift für Physik A Hadrons and Nuclei*, 5(1):17–26, 1921.

[49] Chien-Chih Chiang, Ming-Shyong Tsai, and Min-Hsiung Hon. Luminescent Properties of Cerium-Activated Garnet Series Phosphor: Structure and Temperature Effects. *Journal of The Electrochemical Society*, 155(6):B517–B520, 2008.

[50] Qiyue Shao, Yan Dong, Jianqing Jiang, Chao Liang, and Jinhua He. Temperature-dependent photoluminescence properties of (Y, Lu)$_3$Al$_5$O$_{12}$:Ce^{3+} phosphors for white LEDs applications. *Journal of Luminescence*, 131(5):1013–1015, 2011.

[51] Yibo Chen, Menglian Gong, Gang Wang, and Qiang Su. High efficient and low color-temperature white light-emitting diodes with $Tb_3Al_5O_{12}$:Ce^{3+} phosphor. *Applied Physics Letters*, 91(7):1117, 2007.

[52] Joanna M Ogiegło, Arturas Katelnikovas, Aleksander Zych, Thomas Jüstel, Andries Meijerink, and Cees R Ronda. Luminescence and luminescence quenching in Gd_3(Ga, Al)$_5$O$_{12}$ scintillators doped with Ce^{3+}. *The Journal of Physical Chemistry A*, 117(12):2479–2484, 2013.

[53] Jumpei Ueda, Kotaro Aishima, and Setsuhisa Tanabe. Temperature and compositional dependence of optical and optoelectronic properties in Ce^{3+}-doped $Y_3Sc_2Al_{3-x}Ga_xO_{12}$ (x= 0, 1, 2, 3). *Optical Materials*, 35(11):1952–1957, 2013.

[54] Yi Luo and Zhiguo Xia. Effect of Al/Ga Substitution on Photoluminescence and Phosphorescence Properties of Garnet-Type $Y_3Sc_2Ga_{3-x}Al_xO_{12}$:$Ce^{3+}$ Phosphor. *The Journal of Physical Chemistry C*, 118(40):23297–23305, 2014.

[55] Arturas Katelnikovas, Tomas Bareika, Pranciškus Vitta, Thomas Jüstel, Holger Winkler, Aivaras Kareiva, Artras Žukauskas, and Gintautas Tamulaitis. $Y_{3-x}Mg_2AlSi_2O_{12}$: phosphors prospective for warm-white light emitting diodes. *Optical Materials*, 32(9):1261–1265, 2010.

[56] Meriel C Maniquiz, Kyeong Youl Jung, and Sang Mun Jeong. Luminescence Characteristics of $Y_3Al_{5-2y}(Mg, Si)_yO_{12}$:Ce Phosphor Prepared by Spray Pyrolysis. *Journal of The Electrochemical Society*, 157(12):H1135–H1139, 2010.

[57] Haipeng Ji, Le Wang, Maxim S Molokeev, Naoto Hirosaki, Rongjun Xie, Zhaohui Huang, Zhiguo Xia, M Otmar, Lihong Liu, and Victor V Atuchin. Structure evolution and photoluminescence of $Lu_3(Al, Mg)_2(Al, Si)_3O_{12}$:Ce^{3+} phosphors: new yellow-color converters for blue LED-driven solid state lighting. *Journal of Materials Chemistry C*, 4(28):6855–6863, 2016.

[58] Xinghong Gong, Jianhua Huang, Yujin Chen, Yanfu Lin, Zundu Luo, and Yidong Huang. Novel Garnet-Structure $Ca_2GdZr_2(AlO_4)_3$:Ce^{3+} Phosphor and Its Structural Tuning of Optical Properties. *Inorganic Chemistry*, 53(13):6607–6614, 2014.

[59] A Katelnikovas, S Sakirzanovas, D Dutczak, J Plewa, D Enseling, H Winkler, A Kareiva, and T Jüstel. Synthesis and optical properties of yellow emitting garnet phosphors for pcLEDs. *Journal of Luminescence*, 136:17–25, 2013.

[60] A Katelnikovas, J Plewa, D Dutczak, S Möller, D Enseling, H Winkler, A Kareiva, and T Jüstel. Synthesis and optical properties of green emitting garnet phosphors for phosphor-converted light emitting diodes. *Optical Materials*, 34(7):1195–1201, 2012.

[61] Xian Qin, Xiaowang Liu, Wei Huang, Marco Bettinelli, and Xiaogang Liu. Lanthanide-activated phosphors based on $4f$-$5d$ optical transitions: theoretical and experimental aspects. *Chemical Reviews*, 117(5):4488–4527, 2017.

[62] Cornelis R Ronda. *Luminescence: from theory to applications*. John Wiley & Sons, 2007.

[63] Brian Henderson and G Frank Imbusch. *Optical spectroscopy of inorganic solids*, volume 44. Oxford University Press, 2006.

[64] Pieter Dorenbos. Electronic structure and optical properties of the lanthanide activated $RE_3(Al_{1-x}Ga_x)_5O_{12}$ (RE= Gd, Y, Lu) garnet compounds. *Journal of Luminescence*, 134:310–318, 2013.

[65] P. Dorenbos. Relating the energy of the $[Xe]5d^1$ configuration of Ce^{3+} in inorganic compounds with anion polarizability and cation electronegativity. *Physical Review B*, 65:235110, Jun 2002.

[66] P Dorenbos. $5d$-level energies of Ce^{3+} and the crystalline environment. I. Fluoride compounds. *Physical Review B*, 62(23):15640, 2000.

[67] Gary L Miessler and Donald A Tarr. Inorganic Chemistry. Pearson Education. *Upper Saddle River, NJ*, page 345, 2004.

[68] G F Herrmann, J J Pearson, K A Wickersheim, and R A Buchanan. Crystal Field Effects for Ce^{3+} and Yb^{3+} in the Garnets. *Journal of Applied Physics*, 37(3):1312–1313, 1966.

[69] Philip D Rack and Paul H Holloway. The structure, device physics, and material properties of thin film electroluminescent displays. *Materials Science and Engineering: R: Reports*, 21(4):171–219, 1998.

[70] E G Rogers and P Dorenbos. A comparison of the transition metal $3d_1$ crystal field splitting with the lanthanide $5d_1$ crystal field splitting in compounds. *Journal of Luminescence*, 155:135–140, 2014.

[71] Volker Bachmann, Cees Ronda, and Andries Meijerink. Temperature quenching of yellow Ce^{3+} luminescence in YAG:Ce. *Chemistry of Materials*, 21(10):2077–2084, 2009.

[72] K V Ivanovskikh, J M Ogiegło, A Zych, C R Ronda, and A Meijerink. Luminescence Temperature Quenching for Ce^{3+} and Pr^{3+} d-f Emission in YAG and LuAG. *ECS Journal of Solid State Science and Technology*, 2(2):R3148–R3152, 2013.

[73] D J Robbins. The Effects of Crystal Field and Temperature on the Photoluminescence Excitation Efficiency of Ce^{3+} in YAG. *Journal of The Electrochemical Society*, 126(9):1550–1555, 1979.

[74] Alexander Birkel, Kristin A Denault, Nathan C George, Courtney E Doll, Bathylle Hery, Alexander A Mikhailovsky, Christina S Birkel, Byung-Chul Hong, and Ram Seshadri. Rapid microwave preparation of highly efficient Ce^{3+}-substituted garnet phosphors for solid state white lighting. *Chemistry of Materials*, 24(6):1198–1204, 2012.

76

[75] Pieter Dorenbos. Ce^{3+} $5d$-centroid shift and vacuum referred $4f$-electron binding energies of all lanthanide impurities in 150 different compounds. *Journal of Luminescence*, 135:93–104, 2013.

[76] Jiaqing Liu, Xiaojun Wang, Tongtong Xuan, Chunbo Wang, Huili Li, and Zhuo Sun. $Lu_3(Al, Si)_5(O, N)_{12}$:$Ce^{3+}$ phosphors with broad emission band and high thermal stability for white LEDs. *Journal of Luminescence*, 158:322–327, 2015.

[77] Jiyou Zhong, Weiren Zhao, Weidong Zhuang, Fu Du, Yunan Zhou, Yanlin Yu, and Ligen Wang. Selective coordination of N^{3-} and tuning of luminescence in garnet $(Y_{1-x}, La_x)_3(Al, Si)_5(O, N)_{12}$:$Ce^{3+}$ phosphors. *Journal of Alloys and Compounds*, 726:658–663, 2017.

[78] Wei-Ting Chen, Hwo-Shuenn Sheu, Ru-Shi Liu, and J Paul Attfield. Cation-size-mismatch tuning of photoluminescence in oxynitride phosphors. *Journal of the American Chemical Society*, 134(19):8022–8025, 2012.

[79] AL Allred. Electronegativity values from thermochemical data. *Journal of inorganic and nuclear chemistry*, 17(3-4):215–221, 1961.

[80] Anant A. Setlur, William J. Heward, Yan Gao, Alok M. Srivastava, R. Gopi Chandran, and and Madras V. Shankar. Crystal Chemistry and Luminescence of Ce^{3+}-Doped $Lu_2CaMg_2(Si,Ge)_3O_{12}$ and Its Use in LED Based Lighting. *Chemistry of Materials*, 18(14):3314–3322, 2006.

[81] Yuan-Chih Lin, Paul Erhart, Marco Bettinelli, and Maths Karlsson. Vibrational tuning of photoluminescence in Ce^{3+}-doped garnet phosphors. *To be published*, 2018.

[82] Yongfu Liu, Xia Zhang, Zhendong Hao, Yongshi Luo, XiaoJun Wang, and Jiahua Zhang. Crystal structure and luminescence properties of Lu^{3+} and Mg^{2+} incorporated silicate garnet $[Ca_{3-(x+0.06)}Lu_xCe_{0.06}](Sc_{2-y}Mg_y)Si_3O_{12}$. *Journal of Luminescence*, 132(5):1257–1260, 2012.

[83] YX Pan, W Wang, GK Liu, S Skanthakumar, RA Rosenberg, XZ Guo, and Kewen K Li. Correlation between structure variation and luminescence red shift in YAG:Ce. *Journal of Alloys and Compounds*, 488(2):638–642, 2009.

[84] Jiyou Zhong, Weiren Zhao, Weidong Zhuang, Wei Xiao, Yaling Zheng, Fu Du, and Ligen Wang. Origin of spectral blue shift of Lu^{3+}-codoped

YAG:Ce^{3+} phosphor: First-principles study. *ACS Omega*, 2(9):5935–5941, 2017.

[85] Lei Chen, Xiuling Chen, Fayong Liu, Haohong Chen, Hui Wang, Erlong Zhao, Yang Jiang, Ting-Shan Chan, Chia-Hsin Wang, Wenhua Zhang, et al. Charge deformation and orbital hybridization: intrinsic mechanisms on tunable chromaticity of Y$_3$Al$_5$O$_{12}$:Ce^{3+} luminescence by doping Gd^{3+} for warm white LEDs. *Scientific reports*, 5:11514, 2015.

[86] Yasushi Kanke and Alexandra Navrotsky. A Calorimetric Study of the Lanthanide Aluminum Oxides and the Lanthanide Gallium Oxides: Stability of the Perovskites and the Garnets. *Journal of Solid State Chemistry*, 141(2):424–436, 1998.

[87] AA Setlur and AM Srivastava. On the relationship between emission color and Ce^{3+} concentration in garnet phosphors. *Optical Materials*, 29(12):1647–1652, 2007.

[88] Volker Bachmann, Cees Ronda, Oliver Oeckler, Wolfgang Schnick, and Andries Meijerink. Color point tuning for (Sr, Ca, Ba)Si$_2$O$_2$N$_2$:Eu^{2+} for white light LEDs. *Chemistry of Materials*, 21(2):316–325, 2008.

[89] Ana Belén Muñoz-García and Luis Seijo. Structural, electronic, and spectroscopic effects of Ga codoping on Ce-doped yttrium aluminum garnet: First-principles study. *Physical Review B*, 82(18):184118, nov 2010.

[90] Akihiko Nakatsuka, Akira Yoshiasa, and Takamitsu Yamanaka. Cation distribution and crystal chemistry of Y$_3$Al$_{5-x}$Ga$_x$O$_{12}$ ($0 \leq x \leq 5$) garnet solid solutions. *Acta Crystallographica Section B: Structural Science*, 55(3):266–272, 1999.

[91] Luis Seijo and Zoila Barandiarán. $4f$ and $5d$ Levels of Ce^{3+} in D_2 8-fold oxygen coordination. *Optical Materials*, 35(11):1932–1940, 2013.

[92] Luis Seijo and Zoila Barandiaran. Host effects on the optically active $4f$ and $5d$ levels of Ce^{3+} in garnets. *Phys. Chem. Chem. Phys.*, 15(44):19221–19231, 2013.

[93] Yun-Fang Wu, Ya-Han Chan, Yung-Tang Nien, and In-Gann Chen. Crystal structure and optical performance of Al^{3+} and Ce^{3+} codoped Ca$_3$Sc$_2$Si$_3$O$_{12}$ green phosphors for white LEDs. *Journal of the American Ceramic Society*, 96(1):234–240, 2013.

[94] A Kaminska, A Duzynska, M Berkowski, S Trushkin, and A Suchocki. Pressure-induced luminescence of cerium-doped gadolinium gallium garnet crystal. *Physical Review B*, 85(15):155111, 2012.

[95] Philippe F Smet and Jonas J Joos. White light-emitting diodes: Stabilizing colour and intensity. *Nature Materials*, 16(5):500–501, 2017.

[96] Yoon Hwa Kim, Paulraj Arunkumar, Bo Young Kim, Sanjith Unithrattil, Eden Kim, Su-Hyun Moon, Jae Young Hyun, Ki Hyun Kim, Donghwa Lee, Jong-Sook Lee, et al. A zero-thermal-quenching phosphor. *Nature materials*, 16(5):543, 2017.

[97] Liangliang Liang and Xiaogang Liu. Nanocrystals feel the heat. *Nature Photonics*, 12(3):124, 2018.

[98] Charles W Struck and William H Fonger. *Understanding luminescence spectra and efficiency using Wp and related functions*, volume 13. Springer Science & Business Media, 2012.

[99] G Blasse. Thermal quenching of characteristic fluorescence. *The Journal of Chemical Physics*, 51(8):3529–3530, 1969.

[100] Kun Huang and Avril Rhys. Theory of Light Absorption and Non-Radiative Transitions in F-Centres. *Proceedings of the Royal Society of London A: Mathematical, Physical and Engineering Sciences*, 204(1078):406–423, 1950.

[101] Mathijs de Jong, Luis Seijo, Andries Meijerink, and Freddy T Rabouw. Resolving the ambiguity in the relation between Stokes shift and Huang–Rhys parameter. *Physical Chemistry Chemical Physics*, 17(26):16959–16969, 2015.

[102] C W Struck and W H Fonger. Unified model of the temperature quenching of narrow-line and broad-band emissions. *Journal of Luminescence*, 10(1):1–30, 1975.

[103] Ana Belén Muñoz-García, Zoila Barandiarán, and Luis Seijo. Anti-site defects in Ce-doped YAG ($Y_3Al_5O_{12}$): first-principles study on structures and $4f$–$5d$ transitions. *Journal of Materials Chemistry*, 22(37):19888–19897, 2012.

[104] C R Stanek, K J McClellan, M R Levy, C Milanese, and R W Grimes. The effect of intrinsic defects on $RE_3Al_5O_{12}$ garnet scintillator performance. *Nuclear Instruments and Methods in Physics Research Section*

A: Accelerators, Spectrometers, Detectors and Associated Equipment, 579(1):27–30, 2007.

[105] Ivan Venevtsev, Vasilii Khanin, Piotr Rodnyi, Herfried Wieczorek, and Cees Ronda. Temperature quenching of radio-and photoluminescence of $Y_3(Ga, Al)_5O_{12}:Ce^{3+}$ and $Gd_3(Ga, Al)_5O_{12}:Ce^{3+}$ garnet ceramics. *IEEE Transactions on Nuclear Science*, 2018.

[106] Jumpei Ueda, Setsuhisa Tanabe, and Takayuki Nakanishi. Analysis of Ce^{3+} luminescence quenching in solid solutions between $Y_3Al_5O_{12}$ and $Y_3Ga_5O_{12}$ by temperature dependence of photoconductivity measurement. *Journal of Applied Physics*, 110(5):53102, 2011.

[107] E der Kolk, S A Basun, G F Imbusch, and W M Yen. Temperature dependent spectroscopic studies of the electron delocalization dynamics of excited Ce ions in the wide band gap insulator, Lu_2SiO_5. *Applied Physics Letters, 83 (9), 2003*, 2003.

[108] Jumpei Ueda, Pieter Dorenbos, Adrie J J Bos, Andries Meijerink, and Setsuhisa Tanabe. Insight into the thermal quenching mechanism for $Y_3Al_5O_{12}:Ce^{3+}$ through thermoluminescence excitation spectroscopy. *The Journal of Physical Chemistry C*, 119(44):25003–25008, 2015.

[109] Ivan I Vrubel, Roman G Polozkov, Ivan A Shelykh, Vasilii M Khanin, Piotr A Rodnyi, and Cees R Ronda. Bandgap engineering in yttrium–aluminum garnet with Ga doping. *Crystal Growth & Design*, 17(4):1863–1869, 2017.

[110] Stephen W Allison, J R Buczyna, R A Hansel, D G Walker, and G T Gillies. Temperature-dependent fluorescence decay lifetimes of the phosphor $Y_3(Al_{0.5}Ga_{0.5})_5O_{12}:Ce$ 1%. *Journal of Applied Physics*, 105(3):36105, 2009.

[111] Rachael A Hansel, S W Allison, and D G Walker. Temperature-dependent luminescence of Ce^{3+} in gallium-substituted garnets. *Applied Physics Letters*, 95(11):114102, 2009.

[112] Tadeusz Lesniewski, Sebastian Mahlik, Kazuki Asami, Jumpei Ueda, Marek Grinberg, and Setsuhisa Tanabe. Comparison of quenching mechanisms in $Gd_3Al_{5-x}Ga_xO_{12}:Ce^{3+}$ ($x=3$ and 5) garnet phosphors by photocurrent excitation spectroscopy. *Physical Chemistry Chemical Physics*, 2018.

[113] Jumpei Ueda, Andries Meijerink, Pieter Dorenbos, Adrie JJ Bos, and Setsuhisa Tanabe. Thermal ionization and thermally activated crossover quenching processes for $5d$-$4f$ luminescence in $Y_3Al_{5-x}Ga_xO_{12}$:Pr^{3+}. *Physical Review B*, 95(1):014303, 2017.

[114] MJ Weber. Nonradiative decay from $5d$ states of rare earths in crystals. *Solid State Communications*, 12(7):741–744, 1973.

[115] Yuan-Chih Lin, Marco Bettinelli, Suchinder K. Sharma, A. F. G. van der Meer, Britta Redlich, Adolfo Speghini, and Maths Karlsson. Thermal quenching in the yellow-emitting phosphor YAG:Ce^{3+}. *To be published*, 2018.

[116] D L Dexter and James H Schulman. Theory of concentration quenching in inorganic phosphors. *The Journal of Chemical Physics*, 22(6):1063–1070, 1954.

[117] R K Moore, W B White, and T V Long. Vibrational spectra of the common silicates: I. The garnets. *American Mineralogist*, 56(1-2):54, 1971.

[118] W G Fateley, Neil T McDevitt, and Freeman F Bentley. Infrared and Raman Selection Rules for Lattice Vibrations: The Correlation Method. *Applied Spectroscopy*, 25(2):155–173, mar 1971.

[119] Kazuo Nakamoto. *Infrared and Raman Spectra of Inorganic and Coordination Compounds, Theory and Applications in Inorganic Chemistry*. John Wiley & Sons, 2008.

[120] A M Hofmeister and K R Campbell. Infrared spectroscopy of yttrium aluminum, yttrium gallium, and yttrium iron garnets. *Journal of Applied Physics*, 72(2):638–646, 1992.

[121] K Papagelis, G Kanellis, S Ves, and G A Kourouklis. Lattice Dynamical Properties of the Rare Earth Aluminum Garnets ($RE_3Al_5O_{12}$). *Physica Status Solidi B*, 233(1):134–150, 2002.

[122] K Papagelis and S Ves. Vibrational properties of the rare earth aluminum garnets. *Journal of Applied Physics*, 94(10):6491–6498, 2003.

[123] Daniel C Harris and Michael D Bertolucci. *Symmetry and spectroscopy: an introduction to vibrational and electronic spectroscopy*. Courier Corporation, 1978.

Bibliography

[124] Norman Sheppard. *The historical development of experimental techniques in vibrational spectroscopy.* Wiley Online Library, 2002.

[125] Philip C H Mitchell, Stewart F Parker, Anibal J Ramirez-Cuesta, and John Tomkinson. *Vibrational spectroscopy with neutrons: with applications in chemistry, biology, materials science and catalysis*, volume 3. World Scientific, 2005.

[126] Gordon Leslie Squires. *Introduction to the theory of thermal neutron scattering.* Cambridge university press, 2012.

[127] Roger Pynn. Neutron scattering: a primer. *Los Alamos Science*, 19:1–31, 1990.

[128] ILL :: Neutrons for science : Inelastic neutron scattering. Available at https://www.ill.eu/neutrons-for-society/neutron-techniques/inelastic-neutron-scattering-ins/ (accessed 26 September 2018).

[129] Pubudu S Senanayake, Jon-Paul R Wells, Michael F Reid, Rosa B Hughes-Currie, Giel Berden, Roger J Reeves, and Andries Meijerink. Frequency non-degenerate sequential excitation of the impurity trapped exciton in strontium fluoride crystals doped with ytterbium. *Journal of Applied Physics*, 117(13):133109, 2015.

[130] R.B. Bird, W.E. Stewart, and E.N. Lightfoot. *Transport Phenomena.* Wiley International edition. Wiley, 2007.

[131] Carl W F T Pistorius. The Harmonic Vibration Problem of the Cubic XY_8 Molecule. *Bulletin des Sociétés Chimiques Belges*, 68(10-12):630–642, 1959.

[132] Richard Conger Powell. *Symmetry, group theory, and the physical properties of crystals*, volume 824. Springer, 2010.

[133] N W Ashcroft and N D Mermin. *Solid state physics.* Science: Physics. Saunders College, 1976.

[134] V Monteseguro, P Rodríguez-Hernández, R Vilaplana, FJ Manjón, V Venkatramu, Daniel Errandonea, V Lavín, and Alfonso Munoz. Lattice dynamics study of nanocrystalline yttrium gallium garnet at high pressure. *The Journal of Physical Chemistry C*, 118(24):13177–13185, 2014.

[135] Michael Gaft, Renata Reisfeld, and Gérard Panczer. *Modern luminescence spectroscopy of minerals and materials.* Springer, 2015.

[136] Jose Solé, Luisa Bausa, and Daniel Jaque. *An introduction to the optical spectroscopy of inorganic solids.* John Wiley & Sons, 2005.

[137] Pieter Dorenbos. Modeling the chemical shift of lanthanide $4f$ electron binding energies. *Physical Review B*, 85(16):165107, 2012.

[138] Pieter Dorenbos. A review on how lanthanide impurity levels change with chemistry and structure of inorganic compounds. *ECS Journal of Solid State Science and Technology*, 2(2):R3001–R3011, 2013.

[139] EG Rogers and P Dorenbos. Vacuum energy referred $Ti^{3+/4+}$ donor/acceptor states in insulating and semiconducting inorganic compounds. *Journal of Luminescence*, 153:40–45, 2014.

[140] EG Rogers and P Dorenbos. Vacuum referred binding energy of the single $3d$, $4d$, or $5d$ electron in transition metal and lanthanide impurities in compounds. *ECS Journal of Solid State Science and Technology*, 3(10):R173–R184, 2014.

[141] AJJ Bos. Theory of thermoluminescence. *Radiation Measurements*, 41:S45–S56, 2006.

[142] Koen Van den Eeckhout, Adrie JJ Bos, Dirk Poelman, and Philippe F Smet. Revealing trap depth distributions in persistent phosphors. *Physical Review B*, 87(4):045126, 2013.

[143] Brian C Smith. *Fundamentals of Fourier transform infrared spectroscopy.* CRC press, 2011.

[144] Bernhard Schrader. *Infrared and Raman spectroscopy: methods and applications.* John Wiley & Sons, 2008.

[145] S F Parker, J Tomkinson, A J Ramirez-Cuesta, and D Colognesi. The Tosca user-guide. Technical report, Council for the Central Laboratory of the Research Councils (United Kingdom), 2003.

[146] FEL operating principle - FELIX Laboratory. Available at https://www.ru.nl/felix/about-felix/about-felix/fel-operating-principle/ (accessed 26 September 2018).

[147] E.B. Szarmes. *Classical Theory of Free-Electron Lasers.* IOP Concise Physics: A Morgan & Claypool Publication. Morgan & Claypool Publishers, 2014.

[148] Henry P Freund. *Principles of free-electron lasers.* Springer Science & Business Media, 2012.

[149] D Oepts, A F G der Meer, and P W Van Amersfoort. The free-electron-laser user facility FELIX. *Infrared physics & technology*, 36(1):297–308, 1995.

[150] http://www.ru.nl/felix/about-felix/about-felix/felix-laboratory/ (accessed 26 September 2018).

[151] USB2000+ (Custom) - Ocean Optics. Available at http://oceanoptics.com/wp-content/uploads/USB2000-Operating-Instructions1.pdf (accessed 26 September 2018).

[152] Jose Gracia, Luis Seijo, Zoila Barandiarán, Daniel Curulla, Hans Niemansverdriet, and Wouter van Gennip. *Ab initio* calculations on the local structure and the $4f$–$5d$ absorption and emission spectra of Ce^{3+}-doped YAG. *Journal of Luminescence*, 128(8):1248–1254, 2008.